Coverage Analysis of Joint Localization and Communication in THz Systems with 3D Arrays

N.B. When citing this work, cite the original published paper.

(article starts on next page)

Coverage Analysis of Joint Localization and Communication in THz Systems with 3D Arrays

Pinjun Zheng, Tarig Ballal, *Member, IEEE*, Hui Chen, *Member, IEEE*,
Henk Wymeersch, *Senior Member, IEEE*, and Tareq Y. Al-Naffouri, *Senior Member, IEEE*

Abstract—As a key enabler of Terahertz (THz)-based wireless technologies, large-scale multiple-input-multiple-output systems are well known for their advantages in both communication and localization. Contrary to existing works that mostly focus on planar arrays, this paper first explores the potential of three-dimensional (3D) spatial array structures in joint localization and communication coverage enhancement. We consider a THz-band wireless system where a user is equipped with a 3D array receiving downlink far-field signals from multiple base stations with known positions and orientations over Rician fading channels. First, we derive the constrained Cramér-Rao bound (CCRB) for the localization (i.e., position and orientation estimation) performance, based on which we define the localization coverage metrics. Then, we derive the communication key performance indicators (KPIs) including instantaneous signal-to-noise ratio, outage probability, and ergodic capacity, and define the corresponding coverage metrics. To facilitate localization applications using 3D arrays, a maximum likelihood-based algorithm for joint user equipment (UE) position and orientation estimation is proposed, which is initialized by a least squares-based solution. Our numerical results show that the 3D array configuration offers overall higher coverage than the planar array w.r.t. both localization and communication KPIs, although with minor performance loss in certain UE positions and orientations. The proposed localization algorithm is also verified to be efficient in simulations as it attains the derived CCRB.

Index Terms—three-dimensional (3D) arrays, Terahertz (THz), localization, wireless communication, coverage, constrained Cramér-Rao bound (CCRB).

I. INTRODUCTION

With the increasing demands for higher data traffic in wireless communication, the THz frequency band (0.1-10 THz) is envisioned as a key enabler for future sixth generation (6G) wireless communication systems and beyond [1], [2]. Due to the hundreds of GHz bandwidth available, the THz band is able to achieve Terabit-per-second (Tbps) data rates and massive secure connectivity. In addition to the benefits to communication, larger array size (high angular resolution) and larger bandwidth (high delay resolution) in high-frequency systems also enable high-accuracy localization, which has been extensively explored within multiple-input-multiple-output (MIMO) communication systems [3]–[5]. On the other hand, signals at the THz frequencies are unable to penetrate objects, leading to a more direct relationship between the propagation paths and the environment [6]. It is foreseeable that potential localization-aware applications, such as virtual reality (VR)/augmented reality (AR) [7], unmanned aerial vehicle (UAV) [8], vehicular safety [9], etc., will be considered in future communication systems, and more compact and efficient cooperation paradigms of communication and localization will be continuously explored [10], [11].

In early wireless communication systems (e.g., the first generation (1G) and the second generation (2G) cellular systems), the user's location is usually estimated based on the signal strength and time measurements [12]. Enabled by large antenna arrays in the advanced MIMO systems, angle-based localization methods are widely pursued, as they can avoid tight synchronization requirements and achieve high-accuracy localization [6]. Over the years, a plethora of localization techniques based on one-dimensional (1D) arrays [13], two-dimensional (2D) arrays [4], [14], and arbitrary array configurations [15] have been proposed. Although promising localization results are shown in these works and localization-aware mobile network deployment solutions are proposed [16], the localization coverage issue is rarely discussed, which is a practical issue in real localization scenarios. In the far-field and asynchronous scenarios without geometrical constraints,[1] at least two BSs with line-of-sight (LOS) paths are needed for localization (e.g., based on uplink AOAs).[2] Hence, the localization availability is highly limited by the geometrical setup of the user equipment (UE) and BSs. To improve localization coverage, employing 3D arrays is one of the promising options. A localization error bound analysis of 2D and 3D V-shaped arrays is reported in [20], which shows 3D configurations provide better source positioning performance compared to the 2D one for the same number of sensors. Despite the obvious potential of 3D arrays, this concept has

Pinjun Zheng, Tarig Ballal, and Tareq Y. Al-Naffouri are with the Division of Computer, Electrical and Mathematical Science & Engineering, King Abdullah University of Science and Technology (KAUST), Thuwal, 23955-6900, KSA. (Email: {pinjun.zheng; tarig.ahmed; tareq.alnaffouri}@kaust.edu.sa). Hui Chen and Henk Wymeersch are with the Department of Electrical Engineering, Chalmers University of Technology, 41296 Gothenburg, Sweden (Email: {hui.chen; henkw}@chalmers.se).

[1] With geometrical constraints, for example, the height of the localization target, it is possible to localize using a single base station (BS). For instance, a robot with a fixed height on the ground can be localized using angle-of-arrival (AOA)/angle-of-departure (AOD) information from a single BS on the ceiling.

[2] Relying on NLOS paths components [17] or the curvature-of-arrival information (i.e., in the near-field model) [18], promising single-BS localization solutions exist. However, stable NLOS paths are not always available [19], and near-field conditions are not satisfied in the scenarios considered in this paper (as shown calculated in Subsection VI-A). In this work, we consider far-field LOS-based 6D localization, where at least 2 BSs are needed.

not yet been widely studied in radio localization due to its impractical physical size. However, we expect this issue to be solved in the THz band thanks to the very small signal wavelengths.[3] Besides, since existing works on 3D array localization are limited to specific array configurations such as the V-shaped arrays in [20], a more general model for 3D array localization is needed.

For THz communication, researchers meet challenges that differ significantly from those in systems operating at lower frequencies. For instance, to overcome the very short communication distances due to severe power limitations and propagation attenuation, efficient THz-band signal processing techniques are needed [2]. A well-known example is the array-of-subarray (AOSA) architecture, i.e., dividing large antenna arrays into multiple subarrays (SAs), which can improve the beamforming gain and energy efficiency, and thus combat the distance problem [21], [22]. Based on hybrid beamforming, different SA structures have been studied, specifically including the fully connected [23], the subconnected [24], and the overlapped subarray [25] structures. However, these works on SA design mainly focus on the interconnection among the radio-frequency chains (RFCs), phase shifters (PSs) and antenna elements (AEs) (i.e., the RFC-PS-AE mapping). To the best of the authors' knowledge, there is still a lack of work exploring the spatial structure of the SAs (i.e., 3D array) in an AOSA system, which is expected to enhance the connectivity and improve the coverage w.r.t. both communication and localization key performance indicators (KPIs) [26].

Coverage is one of the most important performance indicators in evaluating the performance of communication systems. Over the years, many notable advances in coverage analysis have been reported. For example, [27] presented a general framework to evaluate the coverage and rate performance in mmWave cellular networks. The authors of [28] developed a novel framework characterizing the sensing and communication coverage probability and ergodic capacity in joint communication and sensing networks. For the coexisting radio frequency and THz finite indoor network, a coverage and rate analysis is reported in [29]. Although those works have developed rigorous and tractable models for network-wide performance analysis based on tools such as stochastic geometry, there is still a literature gap in 3D coverage analysis of specific deterministic scenarios involving joint localization and communication systems.

In this paper, we consider a downlink far-field THz-band MIMO wireless system with multiple BSs and a single UE. Localization and communication coverage performance are evaluated jointly over a Rician fading channel, which has been shown to be a good fit for empirical data in the THz band [30]. The UE is equipped with a 3D array of subarrays with arbitrary but known relative element positions and subarray orientations. Each SA is arranged in a 2D space (i.e., a planar SA). Our investigation reveals that leveraging such 3D array configurations in THz wireless systems can enhance the coverage and improve both localization and communication

KPIs relative to the conventional 2D (or planar) structures. Furthermore, to show the practical usability of 3D arrays in radio localization, we propose a maximum likelihood estimation (MLE) algorithm for joint position and orientation estimation for a UE equipped with a 3D array, and an ad-hoc initialization method based on least-square estimation (LSE). The main contributions of this paper are as follows:

- Based on the CCRB, we derive the position error bound (PEB) and orientation error bound (OEB) for the underlying localization problem, and the localization coverage is then defined.
- To explore the communication performance of different array configurations (i.e., 2D arrays and 3D arrays), we derive communication KPIs including instantaneous signal-to-noise ratio (SNR), outage probability, and ergodic capacity. The non-outage coverage and the capacity coverage are then defined.
- To facilitate localization applications using 3D arrays, we propose an efficient method for joint UE position and orientation estimation using Riemannian manifold optimization tools. The proposed method starts with a least-squares (LS) initialization step followed by a maximum likelihood (ML) refinement.
- We assess the derived KPIs and provide a comparative performance analysis of 2D and 3D arrays through numerical simulations. The accuracy of the proposed localization algorithm is verified through the root mean square error (RMSE) comparison with the PEB and OEB.

The paper is organized as follows. Section II introduces the system model. Section III poses the localization problem and derives the localization KPIs including PEB, OEB, and the localization coverage. The communication KPIs are derived in Section IV, including instantaneous SNR, outage probability, ergodic capacity, and the corresponding coverage. A localization algorithm for 3D array configuration is proposed in Section V. Section VI presents simulation results. Finally, the conclusions of the paper are drawn in Section VII. *The simulation examples can be reproduced using code available at https://github.com/ZPinjun/3D_array_joint_Loc_and_Com.*

Notations: A bold lowercase letter $\mathbf{x}$ denotes the column vector, a bold capital letter $\mathbf{X}$ denotes the matrix. $[\mathbf{x}]_i$ represents the i-th entry of the vector $\mathbf{x}$, and $[\mathbf{X}]_{i,j}$ represents the entry in the i-th row and j-th column of the matrix $\mathbf{X}$. The superscripts $(\cdot)^\mathsf{T}$, $(\cdot)^*$, and $(\cdot)^\mathsf{H}$ stand for transpose, conjugate, and conjugate transpose operations, respectively. $\mathrm{Re}(\cdot)$ denotes the operation of taking the real part, and $\angle\cdot$ denotes the operation of taking the phase.

II. SYSTEM MODEL

We consider a far-field downlink scenario with M BSs and one UE, as shown in Fig. 1-(a). The positions and orientations of the BSs are known in a global coordinate system (GCS). Each BS is equipped with a planar array and is connected to an independent RFC.[4] By adopting a 3D AOSA structure, the array of the UE consists of N planar SAs arranged in a

---

[3]For example, a 10×10 half-wavelength spaced array of a $140\,\mathrm{GHz}$ system can be fitted into a $1\,\mathrm{cm}^2$ area, while the same footprint can only support a 2×2 array at the frequency of $28\,\mathrm{GHz}$.

[4]Since we focus on a single UE, deploying one RFC at each BS is sufficient.
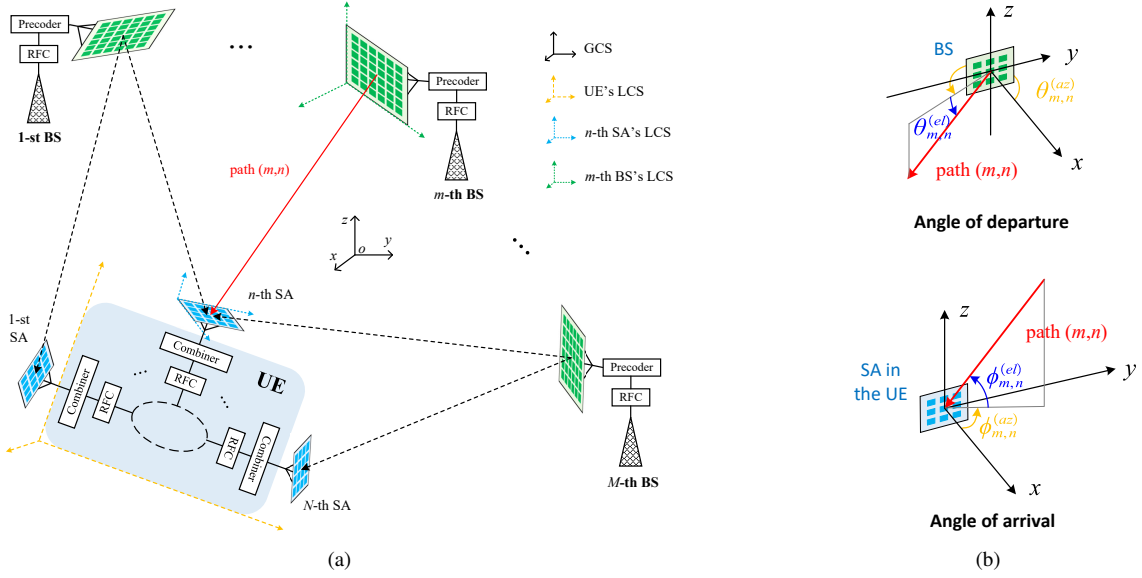
Fig. 1: Illustration of the considered geometric model. (a) A downlink MIMO wireless system with multiple BSs and one UE equipped with a 3D array. (b) The geometry of the azimuth and elevation components of the AOD and AOA.

3D space with fixed relative positions and orientations. Each SA is connected to an independent RFC. Both localization (i.e., determining the position and orientation of the UE) and communication functions are considered is this system.

A. Geometric Model

The m-th BS is deployed at position $\mathbf{p}_{\mathrm{B},m} \in \mathbb{R}^{3\times 1}$, $m = 1, \ldots, M$. It is equipped with a planar antenna array of $N_{\mathrm{B},m}$ elements and oriented according to the rotation matrix $\mathbf{R}_{\mathrm{B},m} \in \mathbb{R}^{3\times 3}$. The position and orientation of the UE in the GCS are denoted as $\mathbf{p}_{\mathrm{U}} \in \mathbb{R}^{3\times 1}$ and $\mathbf{R}_{\mathrm{U}} \in \mathbb{R}^{3\times 3}$, respectively. Without loss of generality, we set $\mathbf{p}_{\mathrm{U}}$ as the origin of the UE's local coordinate system (LCS). The *known* position and orientation of the n-th SA in UE's LCS are denoted as $\mathbf{p}_{\mathrm{S},n}^{\mathrm{UE}} \in \mathbb{R}^{3\times 1}$ and $\mathbf{R}_{\mathrm{S},n}^{\mathrm{UE}} \in \mathbb{R}^{3\times 3}$ respectively, $n = 1, \ldots, N$. Specifically, $\mathbf{p}_{\mathrm{S},n}^{\mathrm{UE}}$ represents the location of the origin of the n-th SA's LCS in UE's LCS. The number of elements of the n-th SA of the UE is denoted as $N_{\mathrm{S},n}$.

All the rotation matrices are constrained in the group of 3D rotations SO(3) [31] defined as

$$\mathrm{SO(3)} = \{\mathbf{R}|\mathbf{R}^{\mathsf{T}}\mathbf{R} = \mathbf{I}_3, \det(\mathbf{R}) = 1\}. \tag{1}$$

A rotation matrix represents the rotation relationship between the GCS and a LCS. For example, for a vector $\mathbf{d}$ in the GCS, we can express its coordinates in the UE's and the n-th SA's LCS as

$$\mathbf{d}^{\mathrm{UE}} = \mathbf{R}_{\mathrm{U}}^{\mathsf{T}}\mathbf{d}, \ \mathbf{d}^{\mathrm{SA},n} = \left(\mathbf{R}_{\mathrm{S},n}^{\mathrm{UE}}\right)^{\mathsf{T}}\mathbf{R}_{\mathrm{U}}^{\mathsf{T}}\mathbf{d}, \ n = 1, 2, \ldots, N.$$

Similarly, the position of the n-th SA (i.e., the origin of the n-th SA's LCS) in the GCS can be expressed as $\mathbf{p}_{\mathrm{S},n} = \mathbf{p}_{\mathrm{U}} + \mathbf{R}_{\mathrm{U}}\mathbf{p}_{\mathrm{S},n}^{\mathrm{UE}}$.

When a link is established between the m-th BS and the n-th SA, the directions of the path can be represented by the AOD from the transmitting side (BS) or the AOA from the receiving side (UE). In 3D space, the AOD consists of a pair of

azimuth angle $\theta_{m,n}^{(\mathrm{az})}$ and elevation angle $\theta_{m,n}^{(\mathrm{el})}$, while the AOA pair consists of an azimuth angle $\phi_{m,n}^{(\mathrm{az})}$ and an elevation angle $\phi_{m,n}^{(\mathrm{el})}$, as visualized in Fig. 1-(b). Another way of expressing the AOA and the AOD is the direction vector. For example, in the m-th BS's LCS, the direction vector from the m-th BS pointing towards n-th SA is given by

$$\mathbf{t}_n^{\mathrm{BS},m} = \begin{bmatrix} \cos(\theta_{m,n}^{(\mathrm{az})})\cos(\theta_{m,n}^{(\mathrm{el})}) \\ \sin(\theta_{m,n}^{(\mathrm{az})})\cos(\theta_{m,n}^{(\mathrm{el})}) \\ \sin(\theta_{m,n}^{(\mathrm{el})}) \end{bmatrix}. \tag{2}$$

This direction vector $\mathbf{t}_n^{\mathrm{BS},m}$ is equivalent to the AOD, and the inverse transformation is given by

$$\theta_{m,n}^{(\mathrm{az})} = \operatorname{atan2}\left(\left[\mathbf{t}_n^{\mathrm{BS},m}\right]_1, \left[\mathbf{t}_n^{\mathrm{BS},m}\right]_2\right), \tag{3}$$

$$\theta_{m,n}^{(\mathrm{el})} = \operatorname{asin}\left(\left[\mathbf{t}_n^{\mathrm{BS},m}\right]_3\right). \tag{4}$$

A similar transformation relationship pair can be obtained for AOA and $\mathbf{t}_m^{\mathrm{SA},n}$.

Since we consider a far-field wireless system with M BSs and a single UE with N SAs, we have at most $M \times N$ LOS paths. However, depending on the positions and orientations of the corresponding BSs and SAs, some of these paths may not exist because of the limited radiation pattern of antennas. We will elaborate on this phenomenon in Subsection II-B.

B. The 3D Array MIMO THz Channel

We consider a far-field scenario where the link distances are larger than the Rayleigh distance [32]. Specifically, we assume that for each pair of visible BS m and SA n, $\|\mathbf{p}_{\mathrm{B},m} - \mathbf{P}_{\mathrm{S},n}\| > \max\{\frac{2D_{\mathrm{B},m}^2}{\lambda_c}, \frac{2D_{\mathrm{S},n}^2}{\lambda_c}\}$, where λ_c denotes the carrier wavelength, and $D_{\mathrm{B},m}$ and $D_{\mathrm{S},n}$ represent the the array apertures of the m-th BS and the n-th SA, respectively. For each visible BS, we consider transmissions of G orthogonal frequency-division multiplexing (OFDM) symbols with K subcarriers [22]. In the localization phase, we assume that

different BSs transmit signals (i.e., G transmissions over the same subcarriers $1, \ldots, K$) at different times, during which the UE state remains unchanged; In the communication phase, only one BS is selected to communicate with the UE based on the localization result (The selection rule used in this paper will be specified in Subsection VI-A). Since the OFDM block duration is usually much smaller than the channel coherence time, the channel can be assumed constant over the G transmissions [6], [14].

1) Signal Model: Using analog beamforming, the signal received by the UE at the k-th subcarrier and the g-th transmission from the m-th BS is given by

$$\mathbf{y}_m^{(g)}[k] = \sqrt{P}\mathbf{W}^{(g)}\mathbf{H}_m[k]\mathbf{w}_{\mathrm{B},m}^{(g)}x_m^{(g)}[k] + \mathbf{W}^{(g)}\mathbf{n}^{(g)}[k], \quad (5)$$

where

$$\mathbf{H}_m[k] = \begin{bmatrix} \mathbf{H}_{m,1}[k] \\ \vdots \\ \mathbf{H}_{m,N}[k] \end{bmatrix}, \quad \mathbf{W}^{(g)} = \begin{bmatrix} \mathbf{w}_{\mathrm{S},1}^{(g)\mathsf{T}} & \cdots & \mathbf{0} \\ \vdots & \ddots & \vdots \\ \mathbf{0} & \cdots & \mathbf{w}_{\mathrm{S},N}^{(g)\mathsf{T}} \end{bmatrix}. \quad (6)$$

Here, P is the average transmission power from each BS, $x_m^{(g)}[k]$ is a unit-modulus symbol, $\mathbf{w}_{\mathrm{B},m}^{(g)} \in \mathbb{C}^{N_{\mathrm{B},m}\times 1}$ is the radio frequency (RF) precoder at the m-th BS, $\mathbf{H}_{m,n}[k] \in \mathbb{C}^{N_{\mathrm{S},n}\times N_{\mathrm{B},m}}$ is the channel matrix from the m-th BS to the n-th SA at the k-th subcarrier, $\mathbf{w}_{\mathrm{S},n}^{(g)} \in \mathbb{C}^{N_{\mathrm{S},n}\times 1}$ is the RF combiner at the n-th SA,[5] and $\mathbf{n}^{(g)}[k] \sim \mathcal{CN}(\mathbf{0}, \sigma^2\mathbf{I}_{N_{\mathrm{S}}})$ is a complex additive white Gaussian noise (AWGN) vector with $N_{\mathrm{S}} = \sum_{n=1}^{N} N_{\mathrm{S},n}$. Each element in $\mathbf{w}_{\mathrm{B},m}^{(g)}/\mathbf{w}_{\mathrm{S},n}^{(g)}$ represents a PS with power constraints $|[\mathbf{w}_{\mathrm{B},m}^{(g)}]_i| = 1/\sqrt{N_{\mathrm{B},m}}$, and $|[\mathbf{w}_{\mathrm{S},n}^{(g)}]_j| = 1/\sqrt{N_{\mathrm{S},n}}$.

2) Antenna Radiation Model: In this work, we consider cone antenna radiation pattern which is modeled with a single cone-shaped beam that approximates the main lobe while ignoring the side lobes. According to this approximation, the antenna gain $G_{\mathrm{B},m}^n/G_{\mathrm{S},n}^m$ is given by [34], [35]

$$G_{\mathrm{B},m}^n = \begin{cases} \frac{2}{1-\cos(\vartheta_{\mathrm{B},m}/2)}, & \text{if } \mathrm{acos}(\boldsymbol{\mu}_{\mathrm{B},m}^\mathsf{T}\mathbf{t}_n^{\mathrm{BS},m}) < \frac{\vartheta_{\mathrm{B},m}}{2}, \\ 0, & \text{otherwise}, \end{cases} \quad (7a)$$

$$G_{\mathrm{S},n}^m = \begin{cases} \frac{2}{1-\cos(\vartheta_{\mathrm{S},n}/2)}, & \text{if } \mathrm{acos}(\boldsymbol{\mu}_{\mathrm{S},n}^\mathsf{T}\mathbf{t}_m^{\mathrm{SA},n}) < \frac{\vartheta_{\mathrm{S},n}}{2}, \\ 0, & \text{otherwise}, \end{cases} \quad (7b)$$

where $\boldsymbol{\mu}_{\mathrm{B},m}$ and $\boldsymbol{\mu}_{\mathrm{S},n}$ are respectively the normal vector of the m-th BS and the n-th SA in their LCSs, and $\vartheta_{\mathrm{B},m}/\vartheta_{\mathrm{S},n}$ denotes the directivity of the antennas of the m-th BS/n-th SA. For instance, for a semi-spherical antenna pattern, $\vartheta = 180^\circ$. In this work, we choose the default normal direction of an array as the x-axis of its LCS. See Fig. 2 for visualization examples of different cone patterns.
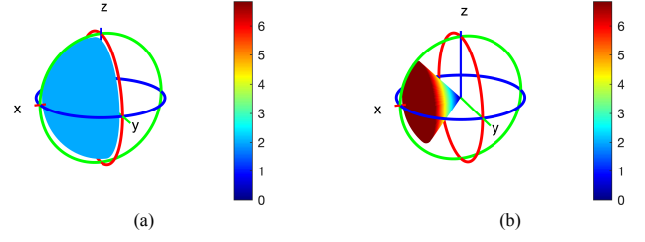
Fig. 2: Example 3D visualizations of the cone antenna gain pattern. (a) $\vartheta = 180^\circ$; (b) $\vartheta = 90^\circ$.

Based on (7), we can define a set $\mathcal{Q}$ below of all available LOS paths based on the visibility of the link between the m-th BS and the n-th SA in the UE:

$$\mathcal{Q} = \Big\{(m,n)\Big| \mathrm{acos}(\boldsymbol{\mu}_{\mathrm{B},m}^\mathsf{T}\mathbf{t}_n^{\mathrm{BS},m}) < \frac{\vartheta_{\mathrm{B},m}}{2},$$
$$\mathrm{acos}(\boldsymbol{\mu}_{\mathrm{S},n}^\mathsf{T}\mathbf{t}_m^{\mathrm{SA},n}) < \frac{\vartheta_{\mathrm{S},n}}{2}, \ m=1,\ldots,M, n=1,\ldots,N\Big\}.$$

To facilitate subsequent discussions, let D denote the cardinality of $\mathcal{Q}$ and assign labels to the elements in the set $\mathcal{Q}$ from 1 to D as $\mathcal{Q} = \{(m_1,n_1),(m_2,n_2),\ldots,(m_D,n_D)\}$. Note that $\mathcal{Q}$ can be identified since each SA and BS is equipped with an independent RFC.

3) Channel Model: In THz wireless communication systems, the LOS path plays a dominant role [1] while the multipath fading effect also exists due to the scattering on aerosols in the atmosphere [36]. A commonly used model for THz wireless propagation captures the LOS path through a deterministic model and generates the multipath components using random processes [22]. As experimentally validated by [30], Rice distribution that models both LOS and none-line-of-sight (NLOS) components is able to achieve a good fit to empirical measurement data in an indoor THz wireless environment. Therefore, we use the Rician fading model to characterize the statistics of the considered THz channel and express the channel sub-matrix $\mathbf{H}_{m,n}[k]$ as [37]

$$\mathbf{H}_{m,n}[k] = \frac{G_{m,n}^k\sqrt{K_r}}{\sqrt{K_r+1}}\bar{\mathbf{H}}_{m,n}[k] + \frac{G_{m,n}^k}{\sqrt{K_r+1}}\tilde{\mathbf{H}}_{m,n}[k]. \quad (8)$$

Here, $\bar{\mathbf{H}}_{m,n}[k]$ is the deterministic LOS component, $\tilde{\mathbf{H}}_{m,n}[k]$ is the random NLOS component, $G_{m,n}^k$ is the path gain, and K_r is the Rician K-factor which represents the ratio between the deterministic and the randomly scattered energies.

The NLOS component of the channel matrix can be expressed as [38]

$$\tilde{\mathbf{H}}_{m,n}[k] = \boldsymbol{\Theta}_{\mathrm{R},n}^{1/2}\hat{\mathbf{H}}_{m,n}[k]\boldsymbol{\Theta}_{\mathrm{T},m}^{1/2}, \quad (9)$$

where the entries of $\hat{\mathbf{H}}_{m,n}[k] \in \mathbb{C}^{N_{\mathrm{S},n}\times N_{\mathrm{B},m}}$ are independent and identically distributed (i.i.d.) $\mathcal{CN}(0,1)$ random variables, and $\boldsymbol{\Theta}_{\mathrm{R},n} \in \mathbb{C}^{N_{\mathrm{S},n}\times N_{\mathrm{S},n}}$ and $\boldsymbol{\Theta}_{\mathrm{T},m} \in \mathbb{C}^{N_{\mathrm{B},m}\times N_{\mathrm{B},m}}$ are receive and transmit correlation matrices, respectively.

The LOS component of the channel matrix, $\bar{\mathbf{H}}_{m,n}[k]$, can be expressed as

$$\bar{\mathbf{H}}_{m,n}[k] = e^{-j(2\pi f_k\tau_{m,n}+\varphi_{m,n})}$$
$$\times \mathbf{a}_{\mathrm{S},n}\left(f_k,\mathbf{t}_m^{\mathrm{SA},n}\right)\mathbf{a}_{\mathrm{B},m}^\mathsf{T}\left(f_k,\mathbf{t}_n^{\mathrm{BS},m}\right), \quad (10)$$

where $\mathbf{a}_{\mathrm{B},m}(f_k, \mathbf{t}_n^{\mathrm{BS},m}) \in \mathbb{C}^{N_{\mathrm{B},m} \times 1}$ and $\mathbf{a}_{\mathrm{S},n}(f_k, \mathbf{t}_m^{\mathrm{SA},n}) \in \mathbb{C}^{N_{\mathrm{S},n} \times 1}$ are respectively the Tx and Rx antenna array response vectors (called beamsteering vectors in this work). The transmitter beamsteering vector can be described as $\left[\mathbf{a}_{\mathrm{B},m}\left(f_k, \mathbf{t}_n^{\mathrm{BS},m}\right)\right]_i = e^{j\frac{2\pi f_k}{c}(\mathbf{t}_n^{\mathrm{BS},m})^{\mathsf{T}}\mathbf{p}_i^{\mathrm{BS},m}}$, where the entries of $\mathbf{p}_i^{\mathrm{BS},m}$ are the coordinates of the i-th AE given in the m-th BS's LCS. The expression of the receiver beamsteering vector $\mathbf{a}_{\mathrm{S},n}$ takes a similar form. In (10), $\varphi_{m,n}$ accounts for the random phase offset introduced by the Tx and Rx hardwares (assumed identical over subcarriers), and $\tau_{m,n}$ is the signal delay of the LOS path given by [6]

$$\tau_{m,n} = \frac{\|\mathbf{p}_{\mathrm{U}} + \mathbf{R}_{\mathrm{U}}\mathbf{p}_{\mathrm{S},n}^{\mathrm{UE}} - \mathbf{p}_{\mathrm{B},m}\|_2}{c} + \rho, \qquad (11)$$

where ρ is the relative clock bias between the BS and the UE and c is the speed of light. We assume that all the BSs are synchronized and that the SAs of the UE share the same clock signal, resulting in a fixed ρ for all paths.

The path gain $G_{m,n}^k$ is given by [39]

$$G_{m,n}^k =$$
$$\begin{cases} \left(\frac{c}{4\pi f_k d_{m,n}}\right)^{\frac{\nu}{2}} e^{-\frac{1}{2}\mathcal{K}(f_k)d_{m,n}}\sqrt{G_{\mathrm{S},n}^m G_{\mathrm{B},m}^n}, & \text{if } (m,n) \in \mathcal{Q}, \\ 0, & \text{if } (m,n) \notin \mathcal{Q}, \end{cases}$$

where the factor $\left(\frac{c}{4\pi f_k d_{m,n}}\right)^{\frac{\nu}{2}}$ accounts for the spreading loss while $e^{-\frac{1}{2}\mathcal{K}(f_k)d_{m,n}}$ accounts for the molecular absorption loss in the THz band. Here, $f_k = f_c + \Delta f_k = f_c + \frac{(2k-1-K)B}{2K}, k = 1, \ldots, K$ is the frequency of the k-th subcarrier, where $f_c = c/\lambda_c$ is the carrier frequency and B is the bandwidth. $d_{m,n}$ is the distance between the m-th BS and the n-th SA, and ν is the path loss exponent. The molecular absorption coefficient, $\mathcal{K}(f_k)$, represents a unique THz fingerprint for different gases and isotopologue, and it can be retrieved from the high-resolution transmission molecular absorption (HITRAN) database [22], [40], [41].

III. LOCALIZATION PERFORMANCE ANALYSIS

The localization problem refers to estimating the position and orientation of the UE based on the received signal $\mathbf{y}_m^{(g)}[k], g = 1, ..., G, k = 1, \ldots, K$ given in (5). In localization performance analysis, we assume identical attenuation coefficients across all subcarriers [6], i.e., $\mathcal{K}(f_k) = \mathcal{K}(f_c)$, thus $G_{m,n}^k = G_{m,n}, \forall k = 1, \ldots, K$. Focusing on the LOS channels, we merge the NLOS component with the AWGN in analyzing the localization error bound. By absorbing the NLOS into the AWGN, the model in (5) becomes

$$\mathbf{y}_m^{(g)}[k] = \underbrace{\sqrt{P}\mathbf{W}^{(g)}\bar{\mathbf{H}}_m[k]\mathbf{w}_{\mathrm{B},m}^{(g)}x_m^{(g)}[k]}_{\boldsymbol{\zeta}_m^{(g)}[k]} + \mathring{\mathbf{n}}_m^{(g)}[k], \qquad (12)$$

where

$$\mathring{\mathbf{n}}_m^{(g)}[k] = \sqrt{P}\mathbf{W}^{(g)}\tilde{\mathbf{H}}_m[k]\mathbf{w}_{\mathrm{B},m}^{(g)}x_m^{(g)}[k] + \mathbf{W}^{(g)}\mathbf{n}^{(g)}[k] \quad (13)$$

$$\bar{\mathbf{H}}_m[k] = \begin{bmatrix} \bar{G}_{m,1}\bar{\mathbf{H}}_{m,1}[k] \\ \vdots \\ \bar{G}_{m,N}\bar{\mathbf{H}}_{m,N}[k] \end{bmatrix}, \ \tilde{\mathbf{H}}_m[k] = \begin{bmatrix} \tilde{G}_{m,1}\tilde{\mathbf{H}}_{m,1}[k] \\ \vdots \\ \tilde{G}_{m,N}\tilde{\mathbf{H}}_{m,N}[k] \end{bmatrix}.$$

Here, $\bar{G}_{m,n} = \frac{G_{m,n}\sqrt{K_r}}{\sqrt{K_r+1}}$, $\tilde{G}_{m,n} = \frac{G_{m,n}}{\sqrt{K_r+1}}$, and $\boldsymbol{\zeta}_m^{(g)}[k]$ in (12) is the noise-free version of the LOS received signal at the UE from the m-th BS. As mentioned in Subsection II-B, different BSs transmit signals to the UE at different times in the localization phase, thus there are MG transmissions. Since we also assumed that the UE state remains unchanged during the localization phase, the deterministic channels $\bar{\mathbf{H}}_m[k]$ in (12) are constant over the MG transmissions.

To facilitate the CCRB derivation, we rewrite the submatrices of $\bar{\mathbf{H}}_m[k]$ as

$$\frac{G_{m,n}\sqrt{K_r}}{\sqrt{K_r+1}}\bar{\mathbf{H}}_{m,n}[k] = \overbrace{h_{m,n}^a e^{-jh_{m,n}^p}}^{h_{m,n}}e^{-j2\pi\Delta f_k\tau_{m,n}}$$
$$\times \mathbf{a}_{\mathrm{S},n}\left(f_k, \mathbf{t}_m^{\mathrm{SA},n}\right)\mathbf{a}_{\mathrm{B},m}^{\mathsf{T}}\left(f_k, \mathbf{t}_n^{\mathrm{BS},m}\right), \quad (14)$$

where $h_{m,n}$ is a complex channel gain with amplitude $h_{m,n}^a = \frac{G_{m,n}\sqrt{K_r}}{\sqrt{K_r+1}}$ and phase $h_{m,n}^p = 2\pi f_c\tau_{m,n} + \varphi_{m,n}$. We now introduce a two-stage localization framework. Subsequently, we derive the PEB, OEB, and the localization coverage metrics based on the CCRB.

A. Two-stage Localization

1) Channel Parameters Estimation: The considered unknown channel parameters consist of AODs at the BSs, AOAs at the SAs in the UE, channel delays, and complex channel gains. These parameters can be stacked in a single vector of the form

$$\boldsymbol{\eta}_{\mathrm{ch}} \triangleq [\underbrace{\boldsymbol{\theta}_{\mathrm{az}}^{\mathsf{T}}, \boldsymbol{\theta}_{\mathrm{el}}^{\mathsf{T}}, \boldsymbol{\phi}_{\mathrm{az}}^{\mathsf{T}}, \boldsymbol{\phi}_{\mathrm{el}}^{\mathsf{T}}, \boldsymbol{\tau}^{\mathsf{T}}}_{\boldsymbol{\eta} \in \mathbb{R}^{5D\times 1}}, \mathbf{h}_a^{\mathsf{T}}, \mathbf{h}_p^{\mathsf{T}}]^{\mathsf{T}} \in \mathbb{R}^{7D\times 1}, \quad (15)$$

where $\boldsymbol{\theta}_{s_1} = [\theta_{m_1,n_1}^{(s_1)}, \ldots, \theta_{m_D,n_D}^{(s_1)}]^{\mathsf{T}}$, $\boldsymbol{\phi}_{s_1} = [\phi_{m_1,n_1}^{(s_1)}, \ldots, \phi_{m_D,n_D}^{(s_1)}]^{\mathsf{T}}$, $\boldsymbol{\tau} = [\tau_{m_1,n_1}, \ldots, \tau_{m_D,n_D}]^{\mathsf{T}}$, $\mathbf{h}_{s_2} = [h_{m_1,n_1}^{s_2}, \ldots, h_{m_D,n_D}^{s_2}]^{\mathsf{T}}$, with $s_1 \in \{\mathrm{az}, \mathrm{el}\}$, $s_2 \in \{a, p\}$, and $(m_i, n_i) \in \mathcal{Q}$. By excluding the nuisance parameters $\mathbf{h}_a$ and $\mathbf{h}_p$, $\boldsymbol{\eta}$ is a vector of parameters that is used for position and orientation estimation.

The objective of the channel parameters estimation stage is to estimate $\boldsymbol{\eta}$ based on the received signal $\mathbf{y}_m^{(g)}[k]$ with all parameters in $\boldsymbol{\eta}_{\mathrm{ch}}$ being unknown. There exists a variety of channel parameter estimators, including ESPRIT [42] and orthogonal matching pursuit [4]. To keep this work focused on the UE position and orientation estimation, we will assume an efficient channel parameter estimation routine that achieves the Cramér-Rao lower bound (CRLB) is available, and the corresponding covariance matrix of the channel parameters is perfectly known.

2) UE Position and Orientation Estimation: In the localization problem, the unknowns of interest are the position and orientation of the UE. Considering also the unknown clock bias ρ as in (11), the localization parameters to be estimated can be grouped in a vector $\mathbf{r} \triangleq \left[\mathbf{p}_{\mathrm{U}}^{\mathsf{T}}, \rho, \mathrm{vec}(\mathbf{R}_{\mathrm{U}})^{\mathsf{T}}\right]^{\mathsf{T}}$.

Estimating the UE position and orientation can be accomplished by estimating the vector $\mathbf{r}$ from the estimated channel parameters $\hat{\boldsymbol{\eta}}$ and the corresponding covariance matrix. The relationships between the channel parameters and the localization parameters are given by (11) and the following

equations, which can be inferred from the geometric model in Subsection II-A,

$$\theta_{m,n}^{(az)} = \text{atan2}\Big(\mathbf{u}_2^\mathsf{T}\mathbf{R}_{B,m}^\mathsf{T}(\mathbf{p}_U + \mathbf{R}_U\mathbf{p}_{S,n}^{UE} - \mathbf{p}_{B,m}),$$
$$\mathbf{u}_1^\mathsf{T}\mathbf{R}_{B,m}^\mathsf{T}(\mathbf{p}_U + \mathbf{R}_U\mathbf{p}_{S,n}^{UE} - \mathbf{p}_{B,m})\Big), \quad (16)$$

$$\theta_{m,n}^{(el)} = \text{asin}\left(\frac{\mathbf{u}_3^\mathsf{T}\mathbf{R}_{B,m}^\mathsf{T}(\mathbf{p}_U + \mathbf{R}_U\mathbf{p}_{S,n}^{UE} - \mathbf{p}_{B,m})}{\|\mathbf{p}_U + \mathbf{R}_U\mathbf{p}_{S,n}^{UE} - \mathbf{p}_{B,m}\|_2}\right), \quad (17)$$

$$\phi_{m,n}^{(az)} = \text{atan2}\Big(-\mathbf{u}_2^\mathsf{T}\left(\mathbf{R}_{S,n}^{UE}\right)^\mathsf{T}\mathbf{R}_U^\mathsf{T}(\mathbf{p}_U + \mathbf{R}_U\mathbf{p}_{S,n}^{UE} - \mathbf{p}_{B,m}),$$
$$-\mathbf{u}_1^\mathsf{T}\left(\mathbf{R}_{S,n}^{UE}\right)^\mathsf{T}\mathbf{R}_U^\mathsf{T}(\mathbf{p}_U + \mathbf{R}_U\mathbf{p}_{S,n}^{UE} - \mathbf{p}_{B,m})\Big), \quad (18)$$

$$\phi_{m,n}^{(el)} = \text{asin}\left(\frac{\mathbf{u}_3^\mathsf{T}\left(\mathbf{R}_{S,n}^{UE}\right)^\mathsf{T}\mathbf{R}_U^\mathsf{T}(\mathbf{p}_U + \mathbf{R}_U\mathbf{p}_{S,n}^{UE} - \mathbf{p}_{B,m})}{-\|\mathbf{p}_U + \mathbf{R}_U\mathbf{p}_{S,n}^{UE} - \mathbf{p}_{B,m}\|_2}\right), \quad (19)$$

where $\mathbf{u}_1 = [1,0,0]^\mathsf{T}$, $\mathbf{u}_2 = [0,1,0]^\mathsf{T}$, $\mathbf{u}_3 = [0,0,1]^\mathsf{T}$.

B. The PEB and OEB

We first derive the CCRB of the localization parameters $\mathbf{r}$, from which the coverage metrics will be derived and analyzed. More details about CRLB can be found in, e.g., [43], [44]. By collecting the observations from all the available paths with labels $(m_i, n_i) \in \mathcal{Q}, i = 1, \ldots, D$, we can write

$$\underbrace{\begin{bmatrix} \left[\mathbf{y}_{m_1}^{(g)}[k]\right]_{n_1} \\ \vdots \\ \left[\mathbf{y}_{m_D}^{(g)}[k]\right]_{n_D} \end{bmatrix}}_{\mathbf{z}^{(g)}[k]} = \underbrace{\begin{bmatrix} \left[\boldsymbol{\zeta}_{m_1}^{(g)}[k]\right]_{n_1} \\ \vdots \\ \left[\boldsymbol{\zeta}_{m_D}^{(g)}[k]\right]_{n_D} \end{bmatrix}}_{\mathbf{m}^{(g)}[k]} + \underbrace{\begin{bmatrix} \left[\mathring{\mathbf{n}}_{m_1}^{(g)}[k]\right]_{n_1} \\ \vdots \\ \left[\mathring{\mathbf{n}}_{m_D}^{(g)}[k]\right]_{n_D} \end{bmatrix}}_{\mathring{\mathbf{n}}^{(g)}[k]}, \quad (20)$$

where $\mathbf{m}^{(g)}[k]$ denotes the noise-free version of the received signal at the k-th subcarrier and the g-th transmission.

Before deriving the CRLB, we determine the statistics of $\mathring{\mathbf{n}}^{(g)}[k]$ in Lemma 1.

Lemma 1. *The noise $\mathring{\mathbf{n}}^{(g)}[k]$ has the following distribution:*

$$\mathring{\mathbf{n}}^{(g)}[k] \sim \mathcal{CN}(\mathbf{0}, \underbrace{diag\{\Sigma_{m_1,n_1}, \ldots, \Sigma_{m_D,n_D}\}}_{\tilde{\boldsymbol{\Sigma}}}), \quad (21)$$

where

$$\Sigma_{m_i,n_i} = \sigma^2\left\|\mathbf{w}_{S,n_i}^{(g)}\right\|_2^2 + \frac{P(G_{m_i,n_i}^k)^2}{1 + K_r}$$
$$\cdot \left\|\boldsymbol{\Theta}_{T,m_i}^{1/2}\mathbf{w}_{B,m_i}^{(g)}x_{m_i}^{(g)}[k]\right\|_2^2 \cdot \left\|\left(\mathbf{w}_{S,n_i}^{(g)}\right)^\mathsf{T}\boldsymbol{\Theta}_{R,n_i}^{1/2}\right\|_2^2,$$
$$i = 1, \ldots, D. \quad (22)$$

Proof. See Appendix A. $\square$

To obtain the CCRB of the localization parameters $\mathbf{r}$, we first derive the Fisher information matrices (FIMs) of the channel parameters $\boldsymbol{\eta}_{ch}$ and $\boldsymbol{\eta}$. The FIM of the channel parameter vector $\boldsymbol{\eta}_{ch}$ can be obtained as in Proposition 1 (For proof see [43, Sec. 3.4]).

Proposition 1. *Given $\{\mathbf{y}_m^{(g)}[k]\}_{m=1,\ldots,M,k=1,\ldots,K,g=1,\ldots,G}$ in (12), the FIM of the unknown channel parameters $\boldsymbol{\eta}_{ch}$ in (15) is given by the Slepian-Bangs formula*

$$\boldsymbol{\mathcal{I}}(\boldsymbol{\eta}_{ch}) = 2\sum_{g=1}^{G}\sum_{k=1}^{K} Re\left(\left(\frac{\partial\mathbf{m}^{(g)}[k]}{\partial\boldsymbol{\eta}_{ch}}\right)^\mathsf{H}\tilde{\boldsymbol{\Sigma}}^{-1}\frac{\partial\mathbf{m}^{(g)}[k]}{\partial\boldsymbol{\eta}_{ch}}\right). \quad (23)$$

Then, we obtain the equivalent Fisher information matrix (EFIM) using AOA, AOD, and channel delays as follows:

$$\boldsymbol{\mathcal{I}}(\boldsymbol{\eta}) = \left(\left[\boldsymbol{\mathcal{I}}(\boldsymbol{\eta}_{ch})^{-1}\right]_{1:5D,1:5D}\right)^{-1}. \quad (24)$$

Now, considering the localization parameters vector $\mathbf{r} = [\mathbf{p}_U^\mathsf{T}, \rho, \text{vec}(\mathbf{R}_U)^\mathsf{T}]^\mathsf{T}$, we can see that $\boldsymbol{\eta}$ is a function of $\mathbf{r}$. The relationships between these two vectors are represented in (11) and (16)–(19). Thus, the FIM with $\mathbf{r}$ as the estimation subject can be obtained as $\boldsymbol{\mathcal{I}}(\mathbf{r}) = \mathbf{T}^\mathsf{T}\boldsymbol{\mathcal{I}}(\boldsymbol{\eta})\mathbf{T}$, where $[\mathbf{T}]_{i,j} = \partial\eta_i/\partial r_j$.

Since $\mathbf{r}$ consists of $\mathbf{R}_U$, which is constrained in SO(3), we have constrained FIM as

$$\boldsymbol{\mathcal{I}}_{\text{const}}^{-1}(\mathbf{r}) = \mathbf{M}(\mathbf{M}^\mathsf{T}\boldsymbol{\mathcal{I}}(\mathbf{r})\mathbf{M})^{-1}\mathbf{M}^\mathsf{T}. \quad (25)$$

Here, $\mathbf{M} \in \mathbb{R}^{13\times7}$ is obtained by collecting the orthonormal basis vectors of the null-space of the gradient matrix of the constraints manifold [17]. A matrix $\mathbf{M}$ can be chosen as

$$\mathbf{M} = \frac{1}{\sqrt{2}}\begin{bmatrix} \sqrt{2}\mathbf{I}_{4\times4} & \mathbf{0}_{4\times1} & \mathbf{0}_{4\times1} & \mathbf{0}_{4\times1} \\ \mathbf{0}_{3\times4} & -\mathbf{c}_3 & \mathbf{0}_{3\times1} & \mathbf{c}_2 \\ \mathbf{0}_{3\times4} & \mathbf{0}_{3\times1} & -\mathbf{c}_3 & -\mathbf{c}_1 \\ \mathbf{0}_{3\times4} & \mathbf{c}_1 & \mathbf{c}_2 & \mathbf{0}_{3\times1} \end{bmatrix}, \quad (26)$$

where $[\mathbf{c}_1, \mathbf{c}_2, \mathbf{c}_3] = \mathbf{R}_U$. Therefore, we have the PEB and the OEB given by

$$\text{PEB} \triangleq \sqrt{\text{tr}([\boldsymbol{\mathcal{I}}_{\text{const}}^{-1}(\mathbf{r})]_{1:3,1:3})}, \quad (27)$$
$$\text{OEB} \triangleq \sqrt{\text{tr}([\boldsymbol{\mathcal{I}}_{\text{const}}^{-1}(\mathbf{r})]_{5:13,5:13})}.$$

Remark 1. *By inspecting (16)–(19), we see that the UE orientation is related to the AODs $(\theta_{m,n}^{(az)}, \theta_{m,n}^{(az)})$ through the term $\mathbf{R}_U\mathbf{p}_{S,n}^{UE}$ only. As the size of the UE is much smaller than the distance between BS and UE, i.e., $\|\mathbf{p}_{S,n}^{UE}\| \ll \|\mathbf{p}_U - \mathbf{p}_{B,m}\|$, changing the orientation $\mathbf{R}_U$ does not cause much difference in the AODs. In other words, AODs carry limited information about the UE's orientation. On the contrary, AOAs carry most of the information regarding the UE rotation. Therefore, a lower OEB is expected in cases with better AOA estimation.*

C. Localization Coverage

Coverage is a metric used to evaluate the overall performance of a localization/communication system [45], [46]. Here, we define the localization coverage as the probability that the PEB/OEB is lower than a threshold ξ^p/ξ^o when the UE is located at random positions $\mathbf{p}_U \in \Omega_p$ and random orientations $\mathbf{R}_U \in \Omega_o$. Here, Ω_p and Ω_o are the sets over which the UE position and orientation vary. More specifically,

the position coverage $R^p(\xi^p)$ and orientation coverage $R^o(\xi^o)$ can be defined as

$$R^p(\xi^p) = \frac{\int_{\Omega_p} \int_{\Omega_o} H(\xi^p - \text{PEB}(\mathbf{p}_U, \mathbf{R}_U)) d\mathbf{p}_U d\mathbf{R}_U}{\int_{\Omega_p} \int_{\Omega_o} d\mathbf{p}_U d\mathbf{R}_U}, \quad (28)$$

$$R^o(\xi^o) = \frac{\int_{\Omega_p} \int_{\Omega_o} H(\xi^p - \text{OEB}(\mathbf{p}_U, \mathbf{R}_U)) d\mathbf{p}_U d\mathbf{R}_U}{\int_{\Omega_p} \int_{\Omega_o} d\mathbf{p}_U d\mathbf{R}_U}, \quad (29)$$

where $H(\cdot)$ is the Heaviside step function (i.e., $H(t) = 1, t \geq 0$ and zero elsewhere), $d\mathbf{p}_U = dp_{Ux} dp_{Uy} dp_{Uz}$, and $d\mathbf{R}_U = d\alpha d\beta d\gamma$.[6]

IV. COMMUNICATION PERFORMANCE ANALYSIS

In this section, we derive the communication KPIs including the instantaneous SNR, the outage probability, and the ergodic capacity. These KPIs are derived assuming that the user is communicating with the m-th BS only. Based on the derived KPIs, the corresponding coverage metrics are defined.

A. Instantaneous SNR

Since the UE maintains multiple RFCs (each SA has an independent RFC), we consider deriving an instantaneous SNR measure for each RFC input upon receiving a signal from a BS. Based on (5) and (6), the instantaneous SNR of the k-th subcarrier for the path from the m-th BS to the n-th UE SA can be defined as

$$\text{SNR}_{m,n}^k \triangleq \frac{P \left| \mathbf{w}_{S,n}^{\mathsf{T}} \mathbf{H}_{m,n}[k] \mathbf{w}_{B,m} \right|^2}{\sigma^2}, \quad (30)$$

where $\text{SNR}_{m,n}^k$ is a random variable whose statistics are characterized by Proposition 2.

Proposition 2. *Define* $Y_{m,n}^k = \left| \mathbf{w}_{S,n}^{\mathsf{T}} \mathbf{H}_{m,n}[k] \mathbf{w}_{B,m} \right|, (m,n) \in \mathcal{Q}$, *then* $Y_{m,n}^k \sim Rician(x|\nu_s, \sigma_s)$, *with a probability density function (PDF) given by*

$$f_{Y_{m,n}^k}(y|\nu_s, \sigma_s) = \frac{y}{\sigma_s^2} e^{\frac{-(y^2 + \nu_s^2)}{2\sigma_s^2}} I_0 \left(\frac{y\nu_s}{\sigma_s^2} \right), \ y > 0, \quad (31)$$

where

$$\nu_s = \left| \frac{G_{m,n}^k \sqrt{K_r}}{\sqrt{K_r + 1}} \mathbf{w}_{S,n}^{\mathsf{T}} \bar{\mathbf{H}}_{m,n}[k] \mathbf{w}_{B,m} \right|, \quad (32)$$

$$\sigma_s^2 = \frac{(G_{m,n}^k)^2 \left\| \mathbf{\Theta}_{T,m}^{1/2} \mathbf{w}_{B,m} \right\|_2^2}{2(K_r + 1)} \left\| \mathbf{w}_{S,n}^{\mathsf{T}} \mathbf{\Theta}_{R,n}^{1/2} \right\|_2^2, \quad (33)$$

and $I_0(x) = \frac{1}{2} \int_0^{2\pi} e^{-x \cos \theta} d\theta$.

Proof. See Appendix B. □

[6]Since $\mathbf{R}_U$ has only three degrees of freedom [31], we denote them as $\{\alpha, \beta, \gamma\}$, which are the Euler angles that will be introduced in subsection VI-A.

B. Outage Probability

We define the outage probability as the probability that the instantaneous SNR of a subcarrier is smaller than a threshold [47], [48]. For the RFC of the n-th SA, the outage probability of the k-th subcarrier for the signal from the m-th BS is given by

$$\begin{aligned} P_{m,n}^{\text{out}}(\gamma_{\text{th}}, k) &= 1, \ \text{if}(m,n) \notin \mathcal{Q}, \\ P_{m,n}^{\text{out}}(\gamma_{\text{th}}, k) &= \mathsf{P}(\text{SNR}_{m,n}^k < \gamma_{\text{th}}) \quad (34) \\ &= \mathsf{P}\left(Y_{m,n}^k < \sqrt{\frac{\gamma_{\text{th}} \sigma^2}{P}} \right) \\ &= F_{Y_{m,n}^k}\left(\sqrt{\frac{\gamma_{\text{th}} \sigma^2}{P}} \right), \ \text{if} \ (m,n) \in \mathcal{Q}, \end{aligned}$$

This follows from (30) and Proposition 2. Here, $F_{Y_{m,n}^k}(\cdot)$ is the cumulative distribution function (CDF) of $Y_{m,n}^k$. Now a signal transmitted from the BS can be received by multiple RFCs in the UE, and so we define the total outage probability at the UE (for transmission from the m-th BS) as $P_{m,k,\gamma_{\text{th}}}^{\text{out}} \triangleq \prod_{n=1}^N P_{m,n}^{\text{out}}(\gamma_{\text{th}}, k)$.

C. Ergodic Capacity

In this work, we assume the channel state information at the receiver (CSIR) and channel distribution information at the transmitter (CDIT) to be perfectly known. As such, we can determine the ergodic capacity (also known as Shannon capacity) for a single transmission from the m-th BS to the UE as [49], [50]

$$C_m = \mathbb{E}\left[\sum_{n=1}^N \sum_{k=1}^K \frac{B}{K} \log_2 \left(1 + \text{SNR}_{m,n}^k \right) \right]. \quad (35)$$

D. Non-Outage Coverage and Capacity Coverage

As mentioned in Subsection II-B, the UE's position and orientation determine which BS is chosen to perform communication with the UE. In other words, m is a function of $\mathbf{p}_U$ and $\mathbf{R}_U$, i.e., $m = m(\mathbf{p}_U, \mathbf{R}_U)$. This function will be specified in Subsection VI-A. Therefore, for each UE position $\mathbf{p}_U$ and orientation $\mathbf{R}_U$, we can denote the total outage probability of k-th subcarrier as $P_{k,\gamma_{\text{th}}}^{\text{out}}(\mathbf{p}_U, \mathbf{R}_U) = P_{m(\mathbf{p}_U, \mathbf{R}_U),k,\gamma_{\text{th}}}^{\text{out}}$, and ergodic capacity as $C(\mathbf{p}_U, \mathbf{R}_U) = C_{m(\mathbf{p}_U, \mathbf{R}_U)}$.

Analogous to the localization coverage metric in Subsection III-C, we define the non-outage coverage and capacity coverage metrics as

$$R_{k,\gamma_{\text{th}}}^{\text{out}}(\xi^{\text{out}}) = \frac{\int_{\Omega_p} \int_{\Omega_o} H(\xi^{\text{out}} - P_{k,\gamma_{\text{th}}}^{\text{out}}(\mathbf{p}_U, \mathbf{R}_U)) d\mathbf{p}_U d\mathbf{R}_U}{\int_{\Omega_p} \int_{\Omega_o} d\mathbf{p}_U d\mathbf{R}_U},$$

$$R^c(\xi^c) = \frac{\int_{\Omega_p} \int_{\Omega_o} H(C(\mathbf{p}_U, \mathbf{R}_U) - \xi^c) d\mathbf{p}_U d\mathbf{R}_U}{\int_{\Omega_p} \int_{\Omega_o} d\mathbf{p}_U d\mathbf{R}_U}.$$

V. LOCALIZATION METHODOLOGY

In this section, the localization algorithm is derived assuming that the following system parameters are given: (1) The positions and orientations of the BSs in the GCS, $\{\mathbf{p}_{B,m}\}_{m=1}^M$, $\{\mathbf{R}_{B,m}\}_{m=1}^M$; (2) The positions and orientations

of the SAs in the UE's LCS, $\{\mathbf{p}_{S,n}^{UE}\}_{n=1}^N$, $\{\mathbf{R}_{S,n}^{UE}\}_{n=1}^N$; (3) The visibility set $\mathcal{Q} = \{(m_1, n_1), (m_2, n_2), \ldots, (m_D, n_D)\}$. As mentioned in subsection III-A, we assume that an efficient channel estimator is applied, which provides unbiased channel parameters estimate $\hat{\boldsymbol{\eta}}$ and the corresponding error covariance matrix $\boldsymbol{\Sigma}$. Now, we focus on the second stage of the localization process.

A. MLE Formulation

The ML criterion is adopted to estimate $\mathbf{r}$ based on $\hat{\boldsymbol{\eta}}$ and $\boldsymbol{\Sigma}$. As $\hat{\boldsymbol{\eta}} \sim \mathcal{N}(\boldsymbol{\eta}, \boldsymbol{\Sigma})$, the log-likelihood function is

$$\ell(\hat{\boldsymbol{\eta}}; \mathbf{p}_U, \rho, \mathbf{R}_U) = \\ -\frac{1}{2}(\hat{\boldsymbol{\eta}} - \boldsymbol{\eta}(\mathbf{p}_U, \rho, \mathbf{R}_U))^\mathsf{T} \boldsymbol{\Sigma}^{-1}(\hat{\boldsymbol{\eta}} - \boldsymbol{\eta}(\mathbf{p}_U, \rho, \mathbf{R}_U)). \quad (36)$$

Now, let $\mathbf{r}_{1:4} = [\mathbf{p}_U^\mathsf{T}, \rho]^\mathsf{T}$, the underlying optimization problem is

$$\hat{\mathbf{r}}_{ML} = \underset{\mathbf{r}_{1:4} \in \mathbb{R}^4, \mathbf{R}_U \in SO(3)}{\arg\max} -\frac{1}{2}(\hat{\boldsymbol{\eta}} - \boldsymbol{\eta}(\mathbf{r}_{1:4}, \mathbf{R}_U))^\mathsf{T} \\ \cdot \boldsymbol{\Sigma}^{-1}(\hat{\boldsymbol{\eta}} - \boldsymbol{\eta}(\mathbf{r}_{1:4}, \mathbf{R}_U)). \quad (37)$$

B. Solving the MLE Problem

Note that (37) is a constrained optimization problem since the rotation matrix $\mathbf{R}_U$ is constrained in the group of 3D rotations $SO(3)$, which is an embedded submanifold of $\mathbb{R}^{3\times 3}$, as defined in (1). In addition, $\mathbf{r}_{1:4}$ lies in the Euclidean space $\mathbb{R}^4$, which is also a manifold. Therefore, we consider using manifold optimization tools to solve (37). To this end, we follow the first-order Riemannian manifold optimization approach [51], [52].

As the product of two embedded submanifolds is still a manifold [52, Sec. 3.2], we can define a product manifold $\mathcal{M}_\mathbf{r}$ as

$$\mathcal{M}_\mathbf{r} \triangleq \mathbb{R}^4 \times SO(3) = \{(\mathbf{r}_{1:4}, \mathbf{R}_U) | \mathbf{r}_{1:4} \in \mathbb{R}^4, \mathbf{R}_U \in SO(3)\}.$$

To simplify the notation, we denote the point in $\mathcal{M}_\mathbf{r}$ as $X = (\mathbf{r}_{1:4}, \mathbf{R}_U)$ such that $\mathbf{r}_{1:4} \in \mathbb{R}^4, \mathbf{R}_U \in SO(3)$.

Similar to the standard steepest descent algorithm, optimization over a manifold is implemented by using the Riemannian gradient. At each iteration, we obtain the Riemannian gradient by projecting the classical gradient to the tangent space $\mathcal{T}_X \mathcal{M}_\mathbf{r}$ of the manifold $\mathcal{M}_\mathbf{r}$. Then, we update the optimization variables in the direction of the Riemannian gradient and retract it from the tangent space $\mathcal{T}_X \mathcal{M}_\mathbf{r}$ onto the manifold $\mathcal{M}_\mathbf{r}$. Mathematically, starting from an initial value $\hat{X}^{(0)}$, the algorithm iterates as follows:

$$\hat{X}^{(k+1)} = \mathcal{R}_{\hat{X}^{(k)}}\left(\epsilon_k \mathcal{P}_{\hat{X}^{(k)}}\left(\left.\frac{\partial\ell(\hat{\boldsymbol{\eta}}; X)}{\partial X}\right|_{X=\hat{X}^{(k)}}\right)\right), \quad (38)$$

where $\mathcal{P}_{\hat{X}^{(k)}}(\cdot)$ is an orthogonal projection from the Euclidean space onto the tangent space $\mathcal{T}_X \mathcal{M}_\mathbf{r}$ at point $X^{(k)}$, $\mathcal{R}_{\hat{X}^{(k)}}(\cdot)$ is a retraction from the tangent space $\mathcal{T}_X \mathcal{M}_\mathbf{r}$ onto the manifold $\mathcal{M}_\mathbf{r}$, and ϵ_k is a suitable step size. The orthogonal projection $\mathcal{P}_{\hat{X}^{(k)}}(\cdot)$, the retraction $\mathcal{R}_{\hat{X}^{(k)}}(\cdot)$, and the gradient $\frac{\partial\ell(\hat{\boldsymbol{\eta}}; X)}{\partial X}$ can be factorized as $\mathcal{P}_{\hat{X}^{(k)}}(\cdot) = \left(\mathcal{P}_{\hat{\mathbf{r}}_{1:4}^{(k)}}(\cdot), \mathcal{P}_{\hat{\mathbf{R}}_U^{(k)}}(\cdot)\right)$, $\mathcal{R}_{\hat{X}^{(k)}}(\cdot) =$

$\left(\mathcal{R}_{\hat{\mathbf{r}}_{1:4}^{(k)}}(\cdot), \mathcal{R}_{\hat{\mathbf{R}}_U^{(k)}}(\cdot)\right)$, $\frac{\partial\ell(\hat{\boldsymbol{\eta}}; X)}{\partial X} = \left(\frac{\partial\ell(\hat{\boldsymbol{\eta}})}{\partial\mathbf{r}_{1:4}}, \frac{\partial\ell(\hat{\boldsymbol{\eta}})}{\partial\mathbf{R}_U}\right)$. The projection and retraction operations of the Riemannian gradient descent algorithm over $\mathcal{M}_\mathbf{r}$ are given by [52, Sec. 7]

$$\mathcal{P}_{\hat{\mathbf{r}}_{1:4}^{(k)}}(\mathbf{u}) = \mathbf{u},$$

$$\mathcal{P}_{\hat{\mathbf{R}}_U^{(k)}}(\mathbf{U}) = \hat{\mathbf{R}}_U^{(k)}\text{skew}\left(\left(\hat{\mathbf{R}}_U^{(k)}\right)^\mathsf{T}\mathbf{U}\right),$$

$$\mathcal{R}_{\hat{\mathbf{r}}_{1:4}^{(k)}}(\mathbf{u}) = \hat{\mathbf{r}}_{1:4}^{(k)} + \mathbf{u},$$

$$\mathcal{R}_{\hat{\mathbf{R}}_U^{(k)}}(\mathbf{U}) = \left(\hat{\mathbf{R}}_U^{(k)} + \mathbf{U}\right)\left(\mathbf{I}_3 + \mathbf{U}^\mathsf{T}\mathbf{U}\right)^{-\frac{1}{2}},$$

where $\text{skew}(\mathbf{A}) = (\mathbf{A} - \mathbf{A}^\mathsf{T})/2$ extracts the skew-symmetric part of a matrix. Let I_K denote the number of iterations, then the computational complexity of (38) is $\mathcal{O}(I_K D)$.

C. Initial Estimation

As the MLE for the localization formulated in this work is a non-convex problem [17], the algorithm might fall into local optima if the initial values are not set properly. Considering this, we propose an LS-based coarse localization method to obtain a proper initial estimate. The proposed initialization method is divided into two parts. We first estimate the UE orientation $\mathbf{R}_U$ and then estimate the UE position & clock bias $\mathbf{r}_{1:4}$ based on the orientation estimate.

1) Initial estimation of orientation using LS: For a path (m_i, n_i) in the set $\mathcal{Q}$, the following relationship holds true

$$\mathbf{R}_U \mathbf{R}_{S,n_i}^{UE} \mathbf{t}_{m_i}^{S,n_i} = -\mathbf{R}_{B,m_i} \mathbf{t}_{n_i}^{B,m_i}, \quad i = 1, 2, \ldots, D. \quad (39)$$

Therefore, letting $\mathbf{A} = -[\mathbf{R}_{B,m_1}\mathbf{t}_{n_1}^{B,m_1}, \ldots, \mathbf{R}_{B,m_D}\mathbf{t}_{n_D}^{B,m_D}]$, $\mathbf{B} = [\mathbf{R}_{S,n_1}^{UE}\mathbf{t}_{m_1}^{S,n_1}, \ldots, \mathbf{R}_{S,n_D}^{UE}\mathbf{t}_{m_D}^{S,n_D}]$, we can formulate an LSE problem for the UE orientation $\mathbf{R}_U$ as

$$\hat{\mathbf{R}}_{U,LS} = \underset{\mathbf{R}_U \in SO(3)}{\arg\min} \|\mathbf{R}_U\mathbf{B} - \mathbf{A}\|_2^2. \quad (40)$$

The optimization problem (40) is a special case of the orthogonal Procrustes problem [53], which admits the closed-form solution

$$\hat{\mathbf{R}}_{U,LS} = \begin{cases} \mathbf{U}\mathbf{V}^\mathsf{T}, & \text{if } \det(\mathbf{U}\mathbf{V}^\mathsf{T}) = 1, \\ \mathbf{U}\mathbf{J}\mathbf{V}^\mathsf{T}, & \text{if } \det(\mathbf{U}\mathbf{V}^\mathsf{T}) = -1, \end{cases} \quad (41)$$

where $\mathbf{J} = [\mathbf{u}_1, \mathbf{u}_2, -\mathbf{u}_3]^\mathsf{T}$ and $\mathbf{U}$ and $\mathbf{V}$ are the unitary basis matrices of the singular value decomposition of $\mathbf{A}\mathbf{B}^\mathsf{T}$, i.e., $\mathbf{A}\mathbf{B}^\mathsf{T} = \mathbf{U}\mathbf{W}\mathbf{V}^\mathsf{T}$ ($\mathbf{W}$ is the diagonal matrix of the singular values).

2) Initial estimation of position & clock bias using LS: Starting with the orientation estimate $\hat{\mathbf{R}}_U$, we can now provide initial estimates of the UE position and clock bias. Specifically, for a path (m_i, n_i) in set $\mathcal{Q}$, we have the following relationships:

$$\mathbf{p}_{B,m_i} + \mathbf{R}_{B,m_i}\mathbf{t}_{n_i}^{B,m_i} \cdot c \cdot (\tau_{m_i,n_i} - \rho) - \hat{\mathbf{R}}_U\mathbf{p}_{S,n}^{UE} = \mathbf{p}_U,$$

$$\mathbf{p}_{B,m_i} - \mathbf{R}_U\mathbf{R}_{S,n_i}^{UE}\mathbf{t}_{m_i}^{S,n_i} \cdot c \cdot (\tau_{m_i,n_i} - \rho) - \hat{\mathbf{R}}_U\mathbf{p}_{S,n}^{UE} = \mathbf{p}_U,$$

$$\forall i = 1, 2, \ldots, D. \quad (42)$$

We can put (42) in a matrix-vector form. Toward that end, let

$$\mathbf{D}_1 = \begin{bmatrix} \mathbf{I}_3 & c\mathbf{R}_{B,m_1}\mathbf{t}_{n_1}^{B,m_1} \\ \mathbf{I}_3 & c\mathbf{R}_{B,m_2}\mathbf{t}_{n_2}^{B,m_2} \\ \vdots & \vdots \\ \mathbf{I}_3 & c\mathbf{R}_{B,m_D}\mathbf{t}_{n_D}^{B,m_D} \end{bmatrix}, \mathbf{D}_2 = \begin{bmatrix} \mathbf{I}_3 & -c\mathbf{R}_U\mathbf{R}_{S,n_1}^{UE}\mathbf{t}_{m_1}^{S,n_1} \\ \mathbf{I}_3 & -c\mathbf{R}_U\mathbf{R}_{S,n_2}^{UE}\mathbf{t}_{m_2}^{S,n_2} \\ \vdots & \vdots \\ \mathbf{I}_3 & -c\mathbf{R}_U\mathbf{R}_{S,n_D}^{UE}\mathbf{t}_{m_D}^{S,n_D} \end{bmatrix},$$

$$\mathbf{b}_1 = \begin{bmatrix} \mathbf{p}_{\text{B},m_1} + \mathbf{R}_{\text{B},m_1}\mathbf{t}_{n_1}^{\text{B},m_1} \cdot c \cdot \tau_{m_1,n_1} - \hat{\mathbf{R}}_{\text{U}}\mathbf{p}_{\text{S},n}^{\text{UE}} \\ \mathbf{p}_{\text{B},m_2} + \mathbf{R}_{\text{B},m_2}\mathbf{t}_{n_2}^{\text{B},m_2} \cdot c \cdot \tau_{m_2,n_2} - \hat{\mathbf{R}}_{\text{U}}\mathbf{p}_{\text{S},n}^{\text{UE}} \\ \vdots \\ \mathbf{p}_{\text{B},m_D} + \mathbf{R}_{\text{B},m_D}\mathbf{t}_{n_D}^{\text{B},m_D} \cdot c \cdot \tau_{m_D,n_D} - \hat{\mathbf{R}}_{\text{U}}\mathbf{p}_{\text{S},n}^{\text{UE}} \end{bmatrix},$$

$$\mathbf{b}_2 = \begin{bmatrix} \mathbf{p}_{\text{B},m_1} - \mathbf{R}_{\text{U}}\mathbf{R}_{\text{S},n_1}^{\text{UE}}\mathbf{t}_{m_1}^{\text{S},n_1} \cdot c \cdot \tau_{m_1,n_1} - \hat{\mathbf{R}}_{\text{U}}\mathbf{p}_{\text{S},n}^{\text{UE}} \\ \mathbf{p}_{\text{B},m_2} - \mathbf{R}_{\text{U}}\mathbf{R}_{\text{S},n_2}^{\text{UE}}\mathbf{t}_{m_2}^{\text{S},n_2} \cdot c \cdot \tau_{m_2,n_2} - \hat{\mathbf{R}}_{\text{U}}\mathbf{p}_{\text{S},n}^{\text{UE}} \\ \vdots \\ \mathbf{p}_{\text{B},m_D} - \mathbf{R}_{\text{U}}\mathbf{R}_{\text{S},n_D}^{\text{UE}}\mathbf{t}_{m_D}^{\text{S},n_D} \cdot c \cdot \tau_{m_D,n_D} - \hat{\mathbf{R}}_{\text{U}}\mathbf{p}_{\text{S},n}^{\text{UE}} \end{bmatrix}.$$

Then we have

$$\underbrace{\begin{bmatrix} \mathbf{D}_1 \\ \mathbf{D}_2 \end{bmatrix}}_{\mathbf{D}} \underbrace{\begin{bmatrix} \mathbf{p}_{\text{U}} \\ \rho \end{bmatrix}}_{\mathbf{r}_{1:4}} = \underbrace{\begin{bmatrix} \mathbf{b}_1 \\ \mathbf{b}_2 \end{bmatrix}}_{\mathbf{b}}, \qquad (43)$$

which has a unique solution given by $\hat{\mathbf{r}}_{1:4,\text{LS}} = (\mathbf{D}^{\mathsf{T}}\mathbf{D})^{-1}\mathbf{D}^{\mathsf{T}}\mathbf{b}$ if $\mathbf{D}$ has full column rank. The full column rank can be guaranteed by the solvability condition proposed in Subsection V-D. The computational complexity of the proposed LS-based initialization computation is $\mathcal{O}(D)$.

D. Solvability Analysis

The localization problem in this section refers to estimating $\mathbf{r} = \left[\mathbf{p}_{\text{U}}^{\mathsf{T}}, \rho, \text{vec}(\mathbf{R}_{\text{U}})^{\mathsf{T}}\right]^{\mathsf{T}} \in \mathbb{R}^{13\times 1}$ based on $\hat{\boldsymbol{\eta}} \in \mathbb{R}^{5D\times 1}$. Note that $\mathbf{R}_{\text{U}}$ has 3 degrees of freedom only; hence, the number of unknowns in $\mathbf{r}$ is reduced to 7. To obtain a unique solution, the number of unknowns should not exceed the number of observations, i.e., $7 \leq 5D$, which requires $D \geq 2$.

It should be noted that a given value of D can be achieved using different combinations of visible BSs and SAs. For instance, $D = 2$ can be achieved with 2 BSs and 1 SA, or alternatively with 1 BS and 2 SAs. The latter case, however, is ill-conditioned under the far-field scenario, as the two paths from the BS to 2 SAs produce very similar AODs and channel delays. Therefore, to guarantee a high localization accuracy, we restrict the solvability condition as: *At least 2 BSs are visible, i.e., the cardinality of the set $\{m_1, \ldots, m_D\}$ in $\mathcal{Q}$ is greater than or equal to 2.*

VI. NUMERICAL SIMULATIONS

A. Simulation Setup

Throughout the simulation examples, the precoder $\mathbf{w}_{\text{B},m}^{(g)}$ and combiner $\mathbf{w}_{\text{S},n}^{(g)}$ are set as follows. When performing localization, we set the elements of $\mathbf{w}_{\text{B},m}^{(g)}$ and $\mathbf{w}_{\text{S},n}^{(g)}$ as PSs with random phases uniformly distributed between 0 and 2π and constant amplitudes $1/\sqrt{N_{\text{B},m}}$ and $1/\sqrt{N_{\text{S},n}}$, respectively. When performing communication, suppose the $\tilde{m}$-th BS is selected to communicate with the UE. We set the n-th SA to always use equal gain combining (EGC) to improve the received SNR for the $\frac{K}{2}$-th subcarrier (assume K is even) from the $\tilde{m}$-th BS. In this case, the combiner is given by [54]

$$[\mathbf{w}_{\text{S},n}(\tilde{m})]_i = \frac{1}{\sqrt{N_{\text{S},n}}}e^{-j\angle[\mathbf{H}_{\tilde{m},n}[\frac{K}{2}]\mathbf{w}_{\text{B},\tilde{m}}]_i}. \qquad (44)$$
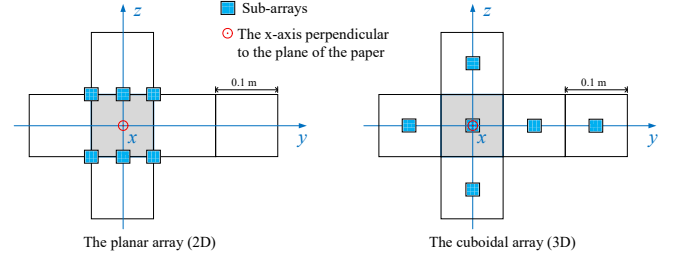

Fig. 3: Illustration of the planar (2D) and cuboidal (3D) array layouts by tiling the cube into a plane.
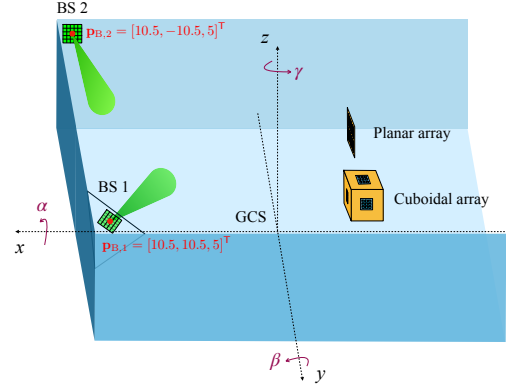

Fig. 4: The indoor scenario considered in simulations, with default parameters provided in Table I.

The precoder $\mathbf{w}_{\text{B},\tilde{m}}$ is set as forming a beam towards the dominant departure direction as [55]

$$[\mathbf{w}_{\text{B},\tilde{m}}]_i = \frac{1}{\sqrt{N_{\text{B},\tilde{m}}}}e^{j\angle[\mathbf{v}_{\max}]_i}, \qquad (45)$$

where $\mathbf{v}_{\max}$ is the right-singular vector of $\mathbf{H}_{\tilde{m}}[\frac{K}{2}]$ that corresponds to the maximum singular value.

In this work, the selection of the $\tilde{m}$-th BS follows the following rule. For each $m = 1, \ldots, M$, we obtain the combiner $\mathbf{w}_{\text{S},n}(m)$ and precoder $\mathbf{w}_{\text{B},m}$ using (44) and (45). Then the single subcarrier SNR, $\text{SNR}_{m,n}^k$, is computed according to (30) using the current channel $\mathbf{H}_{m,n}[k]$. We choose $\tilde{m}$ as the BS that maximizes the sum-rate [50] over all subcarriers and all SAs as

$$\tilde{m} = \arg\max_m \sum_{n=1}^{N}\sum_{k=1}^{K}\frac{B}{K}\log_2(1 + \text{SNR}_{m,n}^k). \qquad (46)$$

In addition, we set both $\boldsymbol{\Theta}_{\text{R},n}$ and $\boldsymbol{\Theta}_{\text{T},m}$ as identity matrices, which means both the receive/transmit antennas are mutually uncorrelated.

We evaluate two different array configurations (2D and 3D), each with 6 SAs. For the 3D array, each SA is placed at the center of a side of a $0.1 \times 0.1 \times 0.1 \text{ m}^3$ cube. On the other hand, the 2D array has all the SAs placed on a plane. For both array configurations, the antenna separation is set as $\lambda_c/2$. Fig. 3 shows the two array layouts where the cube is tiled into a plane. To evaluate the performance of the two array configurations, we consider an indoor scenario with two BSs as shown in Fig. 4, where the UE is placed inside a $20 \times 20 \times 5$ m indoor space (i.e., $-10 < x < 10, -10 < y < 10, 0 < z < 5$). The directivity of antennas are set as $\vartheta_{\text{B},m} = \vartheta_{\text{S},n} =$

TABLE I: Default simulation parameters

Parameter	Value
Propagation Speed c	2.9979×10^8 m/s
Carrier Frequency f_c	140 GHz
Bandwidth B	1000 MHz
# subcarriers K	128
# transmissions G	10
path loss component ν	2
Rician K-factor K_r	4
Transmit Power P	10 mW
Clock Offset ρ	100 ns
Noise PSD N_0	-173.855 dBm/Hz
UE Noise Figure	10 dB
Molecules of Medium	$\{N_2, O_2, H_2O, CO_2, CH_4\}$
Molecules Ratio	$\{76.6\%, 21.0\%, 1.6\%, 0.03\%, 0.77\%\}$
Dimension of BS array	10×10
Dimension of UE's SA	4×4
Positions of BSs	$\mathbf{p}_{B,1} = [10.5, 10.5, 5]^\mathsf{T}$ $\mathbf{p}_{B,2} = [10.5, -10.5, 5]^\mathsf{T}$
Euler Angles of BSs	$\mathbf{o}_{B,1} = [0°, 135°, 45°]^\mathsf{T}$ $\mathbf{o}_{B,2} = [0°, 0°, 90°]^\mathsf{T}$

$180°, \forall m = 1, \dots, M, n = 1, \dots, N$. Other default simulation parameters are listed in Table I. To ensure the validity of the far-field assumption, we calculate the Rayleigh distance of the simulation scenario in this paper. For the link between an arbitrary BS-SA pair, the Rayleigh distance for the BS arrays and the SAs in the UE can be calculated as [32]

$$d_B = \frac{2(10\sqrt{2} \times \frac{\lambda_c}{2})^2}{\lambda_c} = \frac{100c}{f_c} \approx 0.2\,\text{m}, \quad (47)$$

$$d_S = \frac{2(4\sqrt{2} \times \frac{\lambda_c}{2})^2}{\lambda_c} = \frac{16c}{f_c} \approx 0.03\,\text{m}. \quad (48)$$

The BS placements in Table I guarantee that the distance between any visible BS-SA pair is larger than $\max\{d_B, d_S\}$ when the UE is located within the considered space, and so the far-field assumption is valid.

To give an intuitive characterization of the orientation, we use the Euler angles $\mathbf{o} \triangleq [\alpha, \beta, \gamma]^\mathsf{T}$ to represent a rotation matrix $\mathbf{R}$. As such, we use the rotation sequence $\mathbf{R} = \mathbf{R}_z(\gamma)\mathbf{R}_y(\beta)\mathbf{R}_x(\alpha)$, where $\mathbf{R}_x(\alpha)$ denotes a rotation of α degree around the x-axis, and likewise for $\mathbf{R}_y(\beta)$ and $\mathbf{R}_z(\gamma)$. The expressions of these rotation matrices can be found in, e.g., [31].

B. Localization Performance Assessment

1) PEB & OEB vs. UE Position: We first evaluate the distribution of the PEB and OEB across different UE positions for the two array types. We fix the UE orientation as $\alpha = \beta = \gamma = 0°$, and the PEB/OEB is calculated in a $20 \times 20\,\text{m}^2$ area with a $0.2\,\text{m}$ step size and with a fixed z-axis $[\mathbf{p}_U]_3 = 0$. The results are shown in Fig. 5.

For PEB over different UE positions (Fig. 5-(a) and Fig. 5-(b)), we can observe that, in general, the PEB becomes larger as the UE moves away from both BSs. For this specific setup, the planar array appears to have a slightly lower PEB. This is because only a subset of the SAs of the 3D array can receive LOS signals from a BS. In contrast, all the SAs of the planar array enjoy LOS connections with the BSs. From Fig. 5, we can see that the UE gets a worse position estimation
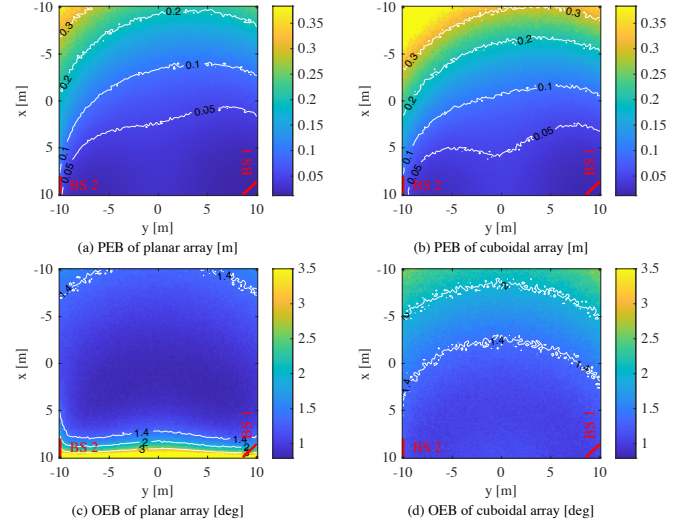

Fig. 5: The PEB and OEB distribution over different UE positions for the planar and cuboidal arrays. We fix UE orientation as $\alpha = \beta = \gamma = 0°$ (towards positive x-axis) and $[\mathbf{p}_U]_3 = 0$.
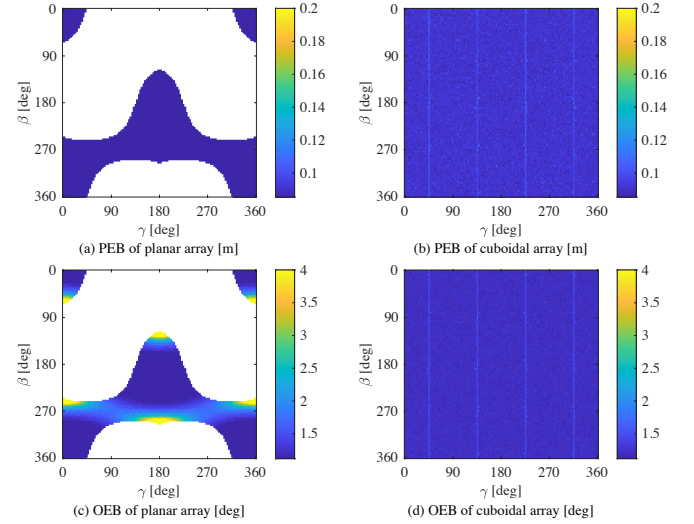

Fig. 6: The PEB and OEB distribution over different UE orientations for the planar and cuboidal arrays. We fix UE position as $\mathbf{p}_U = [0,0,0]^\mathsf{T}$ and $\alpha = 0°$.

performance when located around $y = -10\,\text{m}$ compared with $y = 10\,\text{m}$, due to the less accurate AOD from the BS 2 while the orientation setup of the BS 1 always provides a good AOD estimation.[7] These results reveal that a good AOD helps lower the PEB for both planar and cuboidal array.

For OEB over different UE positions (Fig. 5-(c) and Fig. 5-(d)), we observe that the planar array outperforms the cuboidal array in most of the areas, which can again be explained by the lack of LOS link between some of the cuboidal array's SAs and the BSs. Nonetheless, a striking difference from the PEB distribution is that the OEB of the planar array becomes

[7]Angle estimation of the target at the boresight of the array is usually better than other directions as $\sin(\theta)$ contains more information about the direction when $\theta = 0$ (i.e., $\frac{\partial \sin(\theta)}{\partial \theta}|_{\theta=0} = 1$). Therefore, a bad AOD/AOA means a large angle between the outgoing/incoming direction and the normal direction of the array. On the contrary, a good AOD/AOA means a small angle between the outgoing/incoming direction and the normal direction of the array.
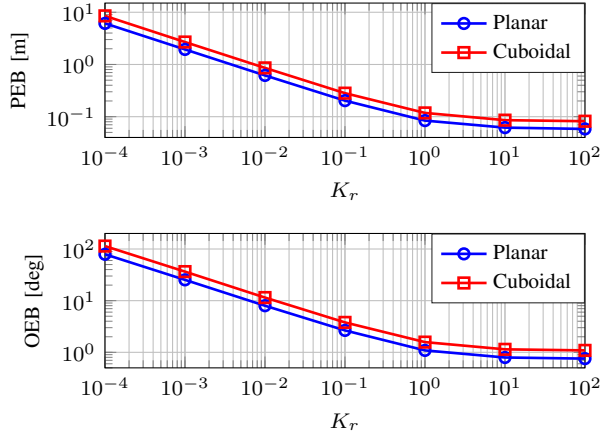
Fig. 7: The PEB and OEB vs. Rician factor K_r for the planar and cuboidal arrays. The UE position and orientation are set as $[0,0,0]^\mathsf{T}$ and $[0°,0°,0°]^\mathsf{T}$, respectively.

Fig. 8: PEB and OEB coverage of the two types of array under $\{2,3,4\}$ BSs with antenna directivity $\vartheta = 180°$.

extremely high around $x = 10\,\mathrm{m}$. This is because the planar array UE gets bad AOA estimation in this area with the selected orientation. In this scenario, the cuboidal array shows more robustness as it benefits from the orientation diversity of its SAs. This result shows that the OEB is highly sensitive to the AOA rather than the AOD, which is consistent with Remark 1.

2) PEB & OEB vs. UE Orientation: Then we evaluate the distribution of the PEB and OEB across different UE orientations for the two array types. We fix the UE position at $\mathbf{p}_\mathrm{U} = [0,0,0]^\mathsf{T}$ and rotate the UE by varying β, γ in the range $[0°, 360°)$ with a $3°$ step while setting $\alpha = 0$. The results are shown in Fig. 6.

From the PEB/OEB over different UE orientations as shown in Fig. 6, we conclude that the 3D array substantially outperforms the 2D array in terms of coverage. Note that localization is impossible in the asynchronous case when the UE can only access fewer than two LOS paths from the BSs. These cases are represented by the white areas in Fig. 6-(a) and Fig. 6-(c) for the planar array, where the PEB and OEB is infinity since performing localization is infeasible. For instance, the planar array does not have a LOS to either BS when β is around $90°$ (i.e., the array points downward), while it has LOS to both BSs when β is around $270°$ (pointing upward). On the other hand, the cuboidal array's performance is fairly consistent across all the test angles. That said, we notice that there are several lines in Fig. 6-(b) and Fig. 6-(d) around $\gamma = 45°$, $\gamma = 135°$, $\gamma = 225°$, and $\gamma = 315°$, with relatively high PEB and OEB for the cuboidal array. This phenomenon occurs because, in these orientations, each BS can only see one or two of the UE SAs, while there are always three SAs visible in other orientations. A final observation vis-a-vis the planar array results in Fig. 6-(a) and Fig. 6-(c) is the presence of several areas with extremely high OEB but low PEB. This is due to same reason of the extremely high OEB in Fig. 5-(c) around $x = 10\,\mathrm{m}$, i.e., bad AOA estimation.

3) PEB & OEB vs. Rician Factor: Next, we test in Fig. 7 the PEB and OEB of the two array types versus the Rician factor K_r with the UE position at $[0,0,0]^\mathsf{T}$ and orientation as
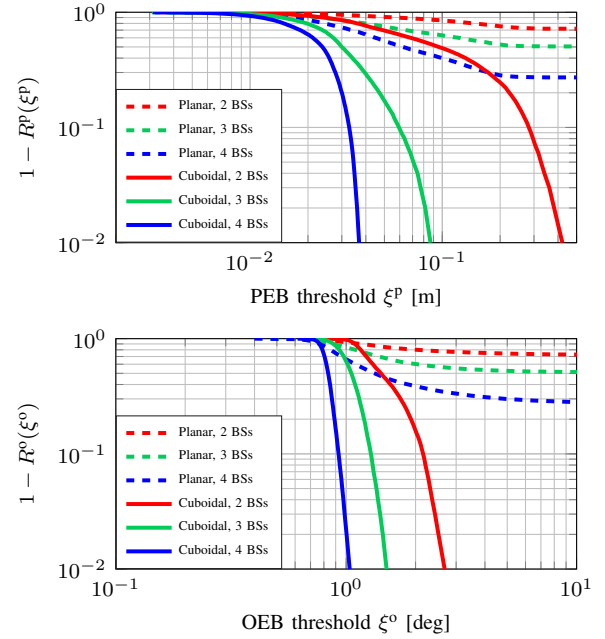
$[0°,0°,0°]^\mathsf{T}$. The planar array keeps a lower PEB and OEB than the cuboidal array because of the full visibility of its SAs in this specific UE position and orientation. Moreover, we see that both the PEB and OEB decrease with increasing K_r before saturating. We can conclude that improving the LOS channel helps lower the localization error bounds. Under the considered system, good localization accuracy can be attained within a practical range of K_r.[8]

4) Localization Coverage Evaluation: Now, we evaluate the localization coverage of the 2D and 3D array configurations defined in (28) and (29). To this end, we randomize the UE position and orientation according to a uniform distribution, namely, $x, y \sim \mathrm{U}(-10, 10)$, $z \sim \mathrm{U}(0, 5)$, and $\alpha, \beta, \gamma \sim \mathrm{U}(0, 360)$, and collect PEB and OEB samples to obtain an empirical CDF. To give a compact view of the PEB/OEB's threshold with the coverage in different orders of magnitude, we plot $1 - R^\mathrm{p}(\xi^\mathrm{p})$ and $1 - R^\mathrm{o}(\xi^\mathrm{o})$ over different threshold ξ^p and ξ^o, which is complementary cumulative distribution function (CCDF). We test the CCDF by performing two simulations: (i) $M = \{2, 3, 4\}$ BSs in a system with a fixed antenna directivity $\vartheta = 180°$, as shown in Fig. 8; (ii) 2 BSs with different antenna directivities ($\vartheta = \{120°, 150°, 180°\}$) as shown in Fig. 9. For the 3 BSs case, we add one BS at location $[-10.5, 10.5, 5]^\mathsf{T}$ with orientation $[0°, 45°, -45°]^\mathsf{T}$; For the 4 BSs case, we add one more BS at location $[-10.5, -10.5, 5]^\mathsf{T}$ with orientation $[0°, 45°, 45°]^\mathsf{T}$. For each case, we repeat 10000 trials to obtain the CCDF curves.

We observe from Fig. 8 and Fig. 9 that the planar array (dashed curves) suffers from limited coverage for all cases. As explained earlier, this is due to the lack of LOS with enough BSs in some specific UE orientation. Take the 4 BSs, $\vartheta = 180°$

---

[8]For instance, the typical Rician factor values of THz links in a shopping mall environment are around $0.1 < K_r < 10$ [56].
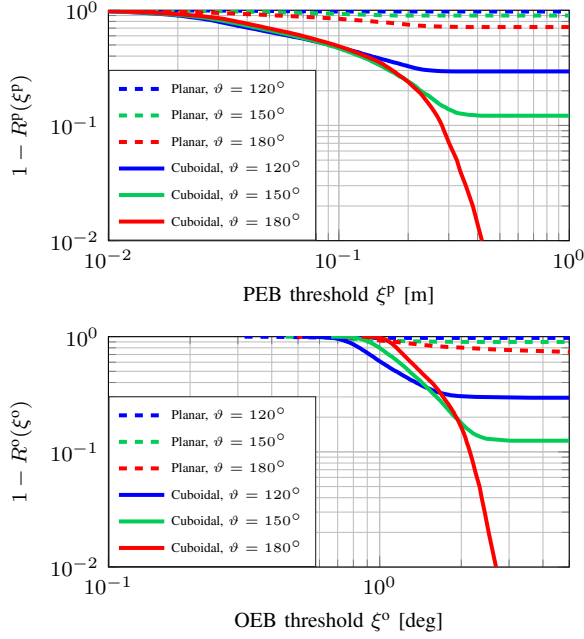
Fig. 9: PEB and OEB coverage of the two types of array under antenna directivity $\vartheta = \{120°, 150°, 180°\}$ with 2 BSs.
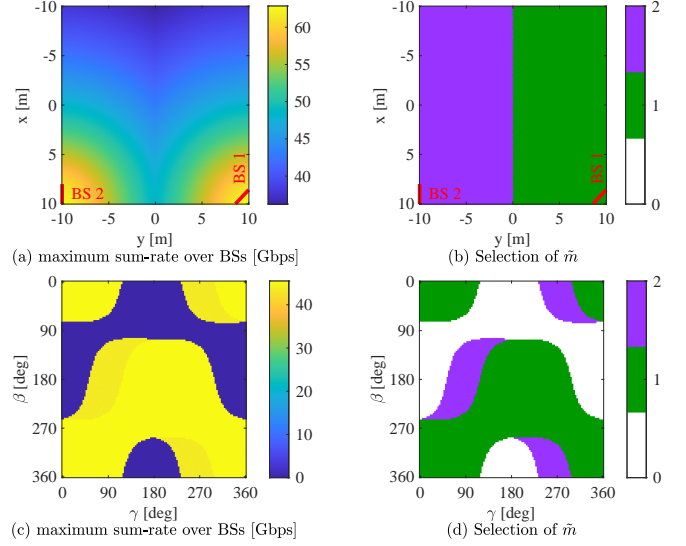

Fig. 10: Maximum sum-rate over different BSs and the communication BS selection results according to (46) using the planar array. The results across different UE positions (fix $[\mathbf{p}_U]_3 = 0$ and orientation $\alpha = \beta = \gamma = 0°$) are presented in (a) and (b), while the results across different UE orientations (fix $\alpha = 0°$ and position $\mathbf{p}_U = [0, 0, 0]^\mathsf{T}$) are presented in (c) and (d). Note that the white areas in (d) represent the UE orientations with which both BSs are invisible.
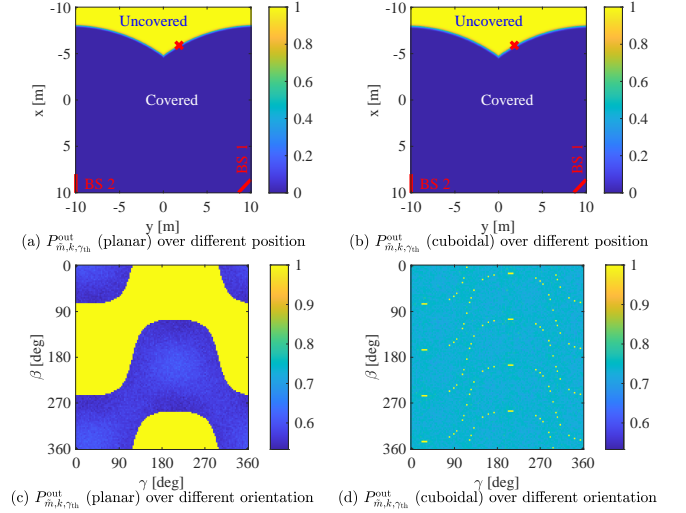

Fig. 11: Outage probability $P^{\text{out}}_{\tilde{m},k,\gamma_{\text{th}}}$ of the planar and cuboidal arrays over different UE positions (fix $[\mathbf{p}_U]_3 = 0$ and orientation $\alpha = \beta = \gamma = 0°$) and orientations (fix $\alpha = 0°$ and position $\mathbf{p}_U = [-5.9, 1.8, 0]^\mathsf{T}$, as marked with a red cross symbol in (a) and (b)), where $k = \frac{K}{2}$, $\gamma_{\text{th}} = 20\,\text{dB}$, and $\tilde{m}$ is selected according to (46).

case with a coverage of 70% (outage of 30%) for example, we have a PEB within about $0.028\,\text{m}$ using the cuboidal array, while the planar array gives a PEB within about $0.173\,\text{m}$. The same result holds in most of the range of ξ^p/ξ^o, revealing that the cuboidal (3D) array is able to achieve better coverage than the planar (2D) array in the practical range of threshold. Besides, we see from Fig. 8 that under the same threshold, the more BSs we deploy, the lower the outage and thus the higher the coverage we can obtain for both 2D and 3D arrays. From Fig. 9, we can see that increasing the antenna directivity (i.e. decreasing ϑ) would improve the localization coverage in the low ξ^o area but degrade the coverage in the high ξ^o area. This is because a more directional antenna heightens the antenna gain and thus produces a lower PEB and OEB in the covered space, which results in the higher coverage in the low ξ^o area. However, at the same time, a narrower beam also causes the shrinkage of the covered space, which results in the coverage limit in the high ξ^o area.

C. Communication KPIs Assessment

As mentioned earlier, only one BS is chosen to communicate with the UE in the communication phase. Before assessing communication KPIs, we test the communication BS selection rule in (46). Taking the planar array as an example, Fig. 10 demonstrates the BS selection results and the corresponding maximum sum-rate across different UE positions and orientations, and this selection rule will be used in the following simulations. It is worth noting that, although different selection rules of $\tilde{m}$ would affect the communication performance, the comparison between the 2D and 3D arrays always yields the same conclusions.

1) Outage Probability vs. UE Position & Orientation: For the outage probability, at first we test the outage probability

$P^{\text{out}}_{\tilde{m},k,\gamma_{\text{th}}}$ of the two types of arrays over different UE positions and orientations. We set $k = \frac{K}{2}$, $\gamma_{\text{th}} = 20\,\text{dB}$, and $\tilde{m}$ is selected according to (46). Other simulation parameters are the same as Subsection VI-B1 and Subsection VI-B2, and the results are shown in Fig. 11. From Fig. 11-(a) and Fig. 11-(b), we can observe that, under both array configurations, the outage probability in most areas is 0 or 1 except for a very narrow boundary. This is because in the THz band, the LOS component is highly dominant, which makes the channel behave with low uncertainty. For the same reason, there is little difference between the outage probability distributions over different UE positions for the two types of arrays. However,
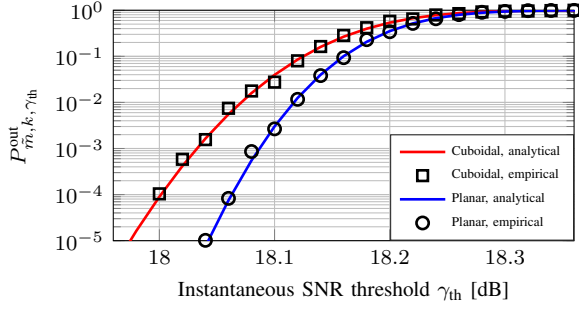
Fig. 12: Outage probability vs. instantaneous SNR threshold with $k = \frac{K}{2}$, $\tilde{m}$ is selected according to (46), and the UE position and orientation are $[-10, 0, 0]^{\mathsf{T}}$ and $[0°, 0°, 0°]^{\mathsf{T}}$.

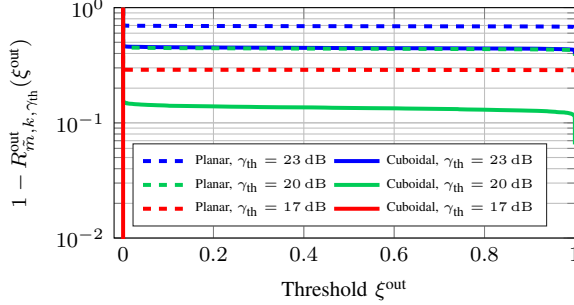Fig. 13: Non-outage coverage of the two types of arrays under instantaneous SNR threshold $\gamma_{\text{th}} = \{17\,\text{dB}, 20\,\text{dB}, 23\,\text{dB}\}$, where $k = \frac{K}{2}$ and $\tilde{m}$ is selected according to (46).

(a) Capacity (planar) over different position

(b) Capacity (cuboidal) over different position

(c) Capacity (planar) over different orientation

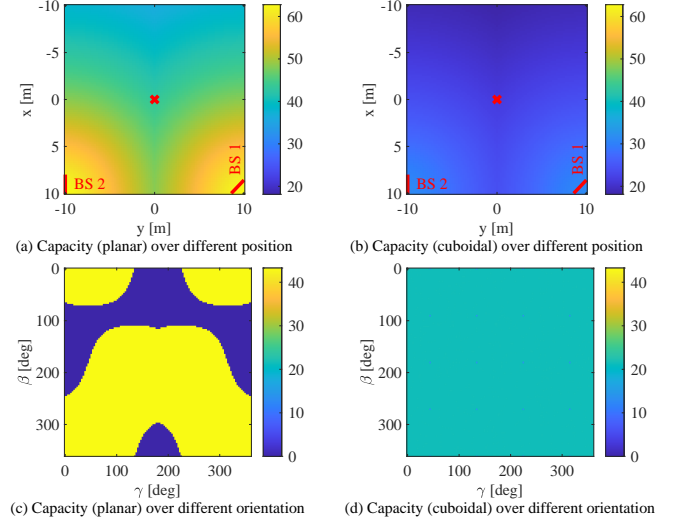(d) Capacity (cuboidal) over different orientation

Fig. 14: Ergodic capacity $C_{\tilde{m}}$ (in units of Gbps) of the planar and cuboidal arrays over different UE positions (fix $z = 0$ and orientation $\alpha = \beta = \gamma = 0°$) and orientations (fix $\alpha = 0°$ and position $\mathbf{p}_{\text{U}} = [0, 0, 0]^{\mathsf{T}}$, as marked with a red cross symbol in (a) and (b)).

when we observe the outage probability distribution over different UE orientations, we see that the planar array has a certain percentage of the uncovered area ($P^{\text{out}}_{\tilde{m}, k, \gamma_{\text{th}}} = 1$) while the cuboidal array has better coverage. Nonetheless, we can clearly see that in the covered UE orientation, the planar array maintains a lower outage probability than the cuboidal one, which shows a trade-off between the peak performance and the overall coverage.

2) Outage Probability vs. Instantaneous SNR Threshold: We further test the outage probability $P^{\text{out}}_{\tilde{m}, k, \gamma_{\text{th}}}$ of the two types of arrays versus instantaneous SNR threshold γ_{th} ranging from 17.96 dB to 18.36 dB with a step size of 0.02 dB. For this simulation, we set $k = \frac{K}{2}$ and the UE position and orientation as $[-10, 0, 0]^{\mathsf{T}}$ and $[0°, 0°, 0°]^{\mathsf{T}}$, respectively. For each γ_{th} point, we evaluate $P^{\text{out}}_{\tilde{m}, k, \gamma_{\text{th}}}$ both analytically and empirically. The result is demonstrated in Fig. 12. We can observe that the planar array is able to provide a lower outage probability in this specific setup, which originates from its full-visibility of all SAs. In general, the outage probability increases as the instantaneous SNR threshold γ_{th} increases.

3) Non-Outage Coverage Evaluation: Now we assess the non-outage coverage of the 2D and 3D array configurations. The simulation is performed under $\gamma_{\text{th}} = \{17\,\text{dB}, 20\,\text{dB}, 23\,\text{dB}\}$, $k = \frac{K}{2}$, and other setup is kept the same as Subsection VI-B4. The result is presented in Fig. 13. We can notice that the non-outage coverage curve is flat as ξ^{out} increases, this is also because the THz channel is LOS-dominant and highly deterministic. The cuboidal array always keeps a higher non-outage coverage than the planar array. Especially, when $\gamma_{\text{th}} = 17\,\text{dB}$, the cuboidal array can cover

all the considered space with a zero outage probability, thus $1 - P^{\text{out}}_{\tilde{m}, k, \gamma_{\text{th}}} = 0$ for all $\xi^{\text{out}} \in [0, 1]$.

4) Ergodic Capacity vs. UE Position & Orientation: For the ergodic capacity, at first we test the ergodic capacity $C_{\tilde{m}}$ of the two types of arrays over different UE positions and orientations. The simulation setup is the same with Subsection VI-B1 and Subsection VI-B2, and the results are shown in Fig. 14. We can observe that, in general, the ergodic capacity becomes lower as the UE moves away from both BSs. For this specific setup, the planar array appears to have a higher capacity across different UE positions compared with the cuboidal array. This is also because of the full-visibility of the SAs of the planar array in this specific orientation. For the ergodic capacity over different UE orientations, it is easy to conclude that the 3D array outperforms the 2D array in terms of coverage, as the 2D array maintains some orientations which are invisible to both BSs and thus results in zero capacity.

5) Ergodic Capacity vs. Rician Factor: Then, we test the ergodic capacity of the two types of arrays versus Rician K-factor for a range from -20 dB to 28 dB with a step size 6 dB under different transmit powers, as shown in Fig. 15. For this simulation, we choose $P = \{5\,\text{mW}, 10\,\text{mW}, 15\,\text{mW}\}$, and the UE position and orientation are $[0, 0, 0]^{\mathsf{T}}$ and $[0°, 0°, 0°]^{\mathsf{T}}$, respectively. We can easily conclude that, the planar array keeps a higher ergodic capacity in this specific setup. It is obvious that the ergodic capacity increases as K_r increases, which implies enlarging the LOS component helps to achieve a higher ergodic sum rate. Besides, in general, the higher the transmit power, the higher the ergodic capacity. The same behaviors of the ergodic capacity w.r.t. K-factor and transmit power/SNR can be found in literature, e.g., [57].

6) Ergodic Capacity Coverage Evaluation: Afterwards, we assess the ergodic capacity coverage of the 2D and 3D array configurations. The simulation is performed under $K_r = \{1, 4, 16\}$, and other setup is the same as Subsection VI-B4. The result is presented in Fig. 16. The ergodic capacity
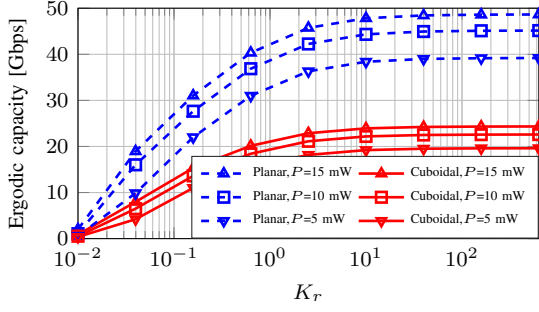
Fig. 15: Ergodic capacity vs. K_r of the two types of array under transmit power $P = \{5\,\text{mW}, 10\,\text{mW}, 15\,\text{mW}\}$.
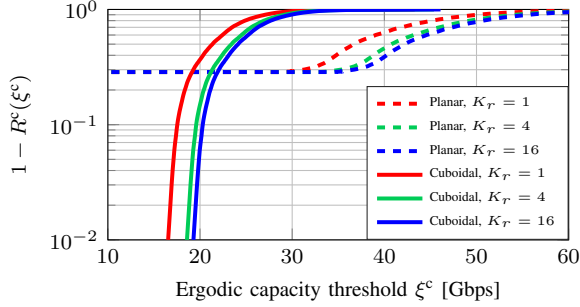

Fig. 16: Ergodic capacity coverage of the two types of arrays under $K_r = \{1, 4, 16\}$.
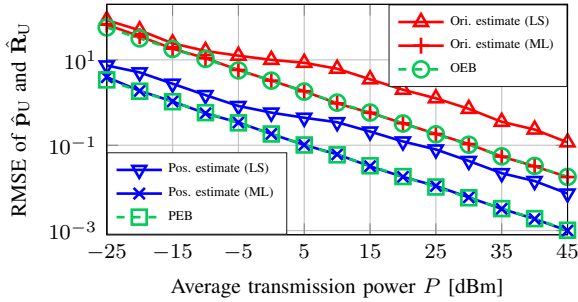

Fig. 17: Position and orientation estimation RMSE vs. the average transmission power. The unit of position RMSE and PEB is meter, and the unit of orientation RMSE and OEB is degree. The UE position and orientation are set as $[1, 3, 2]^\mathsf{T}$ and $[30°, 40°, 50°]^\mathsf{T}$, respectively.

coverage of the planar array is limited to lower than $70\,\%$ for all thresholds while the cuboidal array can achieve a coverage close to $100\,\%$ when the threshold is low enough. It is also observed that the cuboidal array outperforms the planar array in low-capacity threshold regions, while the planar array keeps a better coverage in high-capacity threshold regions. This phenomenon indicates that the cuboidal array provides communication access to more UE positions and orientations at the expense of the loss in peak performance compared to the planar array. By observing the impact of the Rician K-factor, we see that a higher K_r provides a higher coverage of the ergodic capacity, which is consistent with Fig. 15.

D. Localization Algorithm Performance Evaluation

Finally, we evaluate the performance of the proposed estimator using 3D array. Fig. 17 shows the RMSE evaluation of UE position and orientation estimation versus the transmit

power ranging from -25 dBm to 45 dBm with a 5 dBm step size. Both the RMSE of the LS-based initialization and the final estimation based on ML are tested over 300 Monte Carlo trials. To ensure a linear increment of the transmit SNR, here we set $K_r = \infty$ and fixed the noise PSD as the default value. For this simulation, we set the UE position and orientation as $[1, 3, 2]^\mathsf{T}$ and $[30°, 40°, 50°]^\mathsf{T}$, respectively. The algorithm procedures are implemented using the Manopt toolbox [58]. We observe that the accuracy of both estimators is improved by increasing the transmit power. The RMSEs of the MLE are able to reach the PEB/OEB, while the LSE result has a gap to the lower bound. The tightness of ML-based estimator to the PEB and OEB for a practical range shows the efficiency of our proposed estimation algorithm.

VII. CONCLUSION

This paper considered a downlink, far-field THz band MIMO wireless system with multiple BSs and a single UE equipped with a 3D array over Rician fading channel. By deriving the localization error bound in terms of PEB and OEB, and communication KPIs of instantaneous SNR, outage probability, and ergodic capacity, we analyzed and compared the planar and 3D array configuration w.r.t. the coverages of these metrics. A ML-based joint localization algorithm for 3D arrays and a corresponding LS-based initialization method are proposed. The numerical results revealed a higher coverage for 3D array in both localization and communication KPIs given a suitable threshold, and minor performance loss in certain areas compared with the planar array. The proposed localization algorithm is also verified to attain the derived CCRB. This work is instructive for the BS placement optimization, array design, and channel estimation algorithms of the THz localization and communication systems, which can be potential future research directions.

APPENDIX A
PROOF OF LEMMA 1

Suppose $(m, n) \in \mathcal{Q}$, we have

$$\left[\hat{\mathbf{n}}_m^{(g)}[k]\right]_n = \left(\mathbf{w}_{\text{S},n}^{(g)}\right)^\mathsf{T} \mathbf{n}^{(g)}[k] + \\ \sqrt{P}\left(\mathbf{w}_{\text{S},n}^{(g)}\right)^\mathsf{T} \frac{G_{m,n}}{\sqrt{K_r+1}} \mathbf{\Theta}_{\text{R},n}^{1/2} \hat{\mathbf{H}}_{m,n} \mathbf{\Theta}_{\text{T},m}^{1/2} \mathbf{w}_{\text{B},m}^{(g)} x_m^{(g)}[k]. \quad \text{(A-1)}$$

As $\mathbf{n}^{(g)}[k] \sim \mathcal{CN}(\mathbf{0}, \sigma^2 \mathbf{I}_{N_\text{S}})$, we have

$$\left(\mathbf{w}_{\text{S},n}^{(g)}\right)^\mathsf{T} \mathbf{n}^{(g)}[k] \sim \mathcal{CN}\left(\mathbf{0}, \sigma^2 \left\|\mathbf{w}_{\text{S},n}^{(g)}\right\|_2^2\right). \quad \text{(A-2)}$$

As $\left[\hat{\mathbf{H}}_{m,n}\right]_{i,j} \overset{\text{i.i.d.}}{\sim} \mathcal{CN}(0,1)$, we have $\hat{\mathbf{H}}_{m,n} \mathbf{\Theta}_{\text{T},m}^{1/2} \mathbf{w}_{\text{B},m}^{(g)} x_m^{(g)}[k] \sim \mathcal{CN}\left(\mathbf{0}, \left\|\mathbf{\Theta}_{\text{T},m}^{1/2} \mathbf{w}_{\text{B},m}^{(g)} x_m^{(g)}[k]\right\|_2^2 \mathbf{I}_{N_{\text{S},n}}\right)$. Therefore,

$$\sqrt{P}\left(\mathbf{w}_{\text{S},n}^{(g)}\right)^\mathsf{T} \frac{G_{m,n}}{\sqrt{K_r+1}} \mathbf{\Theta}_{\text{R},n}^{1/2} \hat{\mathbf{H}}_{m,n} \mathbf{\Theta}_{\text{T},m}^{1/2} \mathbf{w}_{\text{B},m}^{(g)} x_m^{(g)}[k]$$
$$\sim \mathcal{CN}\left(\mathbf{0}, \frac{P(G_{m,n}^k)^2 \left\|\mathbf{\Theta}_{\text{T},m}^{1/2} \mathbf{w}_{\text{B},m}^{(g)} x_m^{(g)}[k]\right\|_2^2 \cdot \left\|\left(\mathbf{w}_{\text{S},n}^{(g)}\right)^\mathsf{T} \mathbf{\Theta}_{\text{R},n}^{1/2}\right\|_2^2}{K_r+1}\right). \quad \text{(A-3)}$$

Combining (A-2) and (A-3) gives (22).

$$\mathbf{w}_{\text{S},n}^{\mathsf{T}}\mathbf{H}_{m,n}[k]\mathbf{w}_{\text{B},m} = \frac{G_{m,n}^k\sqrt{K_r}}{\sqrt{K_r+1}}\mathbf{w}_{\text{S},n}^{\mathsf{T}}\bar{\mathbf{H}}_{m,n}[k]\mathbf{w}_{\text{B},m} + \frac{G_{m,n}^k}{\sqrt{K_r+1}}\mathbf{w}_{\text{S},n}^{\mathsf{T}}\tilde{\mathbf{H}}_{m,n}[k]\mathbf{w}_{\text{B},m},$$

$$\sim \mathcal{CN}\left(\frac{G_{m,n}^k\sqrt{K_r}}{\sqrt{K_r+1}}\mathbf{w}_{\text{S},n}^{\mathsf{T}}\bar{\mathbf{H}}_{m,n}[k]\mathbf{w}_{\text{B},m}, \frac{(G_{m,n}^k)^2\left\|\boldsymbol{\Theta}_{\text{T},m}^{1/2}\mathbf{w}_{\text{B},m}\right\|_2^2}{K_r+1}\left\|\mathbf{w}_{\text{S},n}^{\mathsf{T}}\boldsymbol{\Theta}_{\text{R},n}^{1/2}\right\|_2^2\right), \tag{A-4}$$

APPENDIX B
PROOF OF PROPOSITION 2

From (A-3), we see

$$\frac{G_{m,n}^k}{\sqrt{K_r+1}}\mathbf{w}_{\text{S},n}^{\mathsf{T}}\tilde{\mathbf{H}}_{m,n}[k]\mathbf{w}_{\text{B},m}$$

$$\sim \mathcal{CN}\left(\mathbf{0}, \frac{(G_{m,n}^k)^2\left\|\boldsymbol{\Theta}_{\text{T},m}^{1/2}\mathbf{w}_{\text{B},m}\right\|_2^2}{K_r+1}\left\|\mathbf{w}_{\text{S},n}^{\mathsf{T}}\boldsymbol{\Theta}_{\text{R},n}^{1/2}\right\|_2^2\right).$$

Therefore, we get (A-4), which follows $Y_{m,n}^k = \left|\mathbf{w}_{\text{S},n}^{\mathsf{T}}\mathbf{H}_{m,n}[k]\mathbf{w}_{\text{B},m}\right| \sim$ Rician$(y|\nu_s, \sigma_s^2)$ with ν_s, σ_s^2 given in (32) and (33).

REFERENCES

[1] H. Sarieddeen, N. Saeed, T. Y. Al-Naffouri, and M.-S. Alouini, "Next generation terahertz communications: A rendezvous of sensing, imaging, and localization," *IEEE Commun. Mag.*, vol. 58, no. 5, pp. 69–75, 2020.

[2] H. Sarieddeen, M.-S. Alouini, and T. Y. Al-Naffouri, "An overview of signal processing techniques for terahertz communications," *Proc. IEEE*, vol. 109, no. 10, pp. 1628–1665, 2021.

[3] N. Garcia, H. Wymeersch, E. G. Larsson, A. M. Haimovich, and M. Coulon, "Direct localization for massive MIMO," *IEEE Trans. Signal Process.*, vol. 65, no. 10, pp. 2475–2487, 2017.

[4] A. Shahmansoori, G. E. Garcia, G. Destino, G. Seco-Granados, and H. Wymeersch, "Position and orientation estimation through millimeter-wave MIMO in 5G systems," *IEEE Trans. Wireless Commun.*, vol. 17, no. 3, pp. 1822–1835, 2018.

[5] P. Zheng, H. Chen, T. Ballal, M. Valkama, H. Wymeersch, and T. Y. Al-Naffouri, "JrCUP: Joint RIS calibration and user positioning for 6G wireless systems," *preprint arXiv:2304.00631*, 2023.

[6] H. Chen, H. Sarieddeen, T. Ballal, H. Wymeersch, M.-S. Alouini, and T. Y. Al-Naffouri, "A tutorial on terahertz-band localization for 6G communication systems," *IEEE Commun. Surveys Tuts.*, May. 2022.

[7] V. Petrov, M. Gapeyenko, S. Paris, A. Marcano, and K. I. Pedersen, "Extended reality (XR) over 5G and 5G-advanced new radio: Standardization, applications, and trends," *preprint arXiv:2203.02242*, 2022.

[8] M. M. Azari, S. Solanki, S. Chatzinotas, and M. Bennis, "THz-empowered UAVs in 6G: Opportunities, challenges, and trade-offs," *IEEE Commun. Mag.*, vol. 60, no. 5, pp. 24–30, 2022.

[9] S. Bartoletti, H. Wymeersch, T. Mach, O. Brunnegård, D. Giustiniano, P. Hammarberg, M. F. Keskin, J. O. Lacruz, S. M. Razavi, J. Rönnblom, F. Tufvesson, J. Widmer, and N. B. Melazzi, "Positioning and sensing for vehicular safety applications in 5G and beyond," *IEEE Commun. Mag.*, vol. 59, no. 11, pp. 15–21, 2021.

[10] S. Dang, O. Amin, B. Shihada, and M.-S. Alouini, "What should 6G be?" *Nat. Electron.*, vol. 3, no. 1, pp. 20–29, 2020.

[11] G. Kwon, A. Conti, H. Park, and M. Z. Win, "Joint communication and localization in millimeter wave networks," *IEEE J. Sel. Top. Signal Process.*, vol. 15, no. 6, pp. 1439–1454, 2021.

[12] J. A. del Peral-Rosado, R. Raulefs, J. A. López-Salcedo, and G. Seco-Granados, "Survey of cellular mobile radio localization methods: From 1G to 5G," *IEEE Commun. Surv. Tutorials*, vol. 20, no. 2, pp. 1124–1148, 2018.

[13] N. Guzey, H. Xu, and S. Jagannathan, "Localization of near-field radio controlled unintended emitting sources in the presence of multipath fading," *IEEE Trans. Instrum. Meas.*, vol. 63, no. 11, pp. 2696–2703, 2014.

[14] L. Kumar, A. Tripathy, and R. M. Hegde, "Robust multi-source localization over planar arrays using MUSIC-group delay spectrum," *IEEE Trans. Signal Process.*, vol. 62, no. 17, pp. 4627–4636, 2014.

[15] F. Belloni, A. Richter, and V. Koivunen, "DoA estimation via manifold separation for arbitrary array structures," *IEEE Trans. Signal Process.*, vol. 55, no. 10, pp. 4800–4810, 2007.

[16] A. Albanese, V. Sciancalepore, A. Banchs, and X. Costa-Pérez, "LOKO: Localization-aware roll-out planning for future mobile networks," *preprint arXiv: 2201.04051*, 2022.

[17] M. A. Nazari, G. Seco-Granados, P. Johannisson, and H. Wymeersch, "MmWave 6D radio localization with a snapshot observation from a single BS," *IEEE Trans. Veh. Technol.*, pp. 1–14, 2023.

[18] A. Elzanaty, A. Guerra, F. Guidi, and M.-S. Alouini, "Reconfigurable intelligent surfaces for localization: Position and orientation error bounds," *IEEE Trans. Signal Process.*, vol. 69, pp. 5386–5402, 2021.

[19] Y. Ge, H. Khosravi, F. Jiang, H. Chen, S. Lindberg, P. Hammarberg, H. Kim, O. Brunnegård, O. Eriksson, B.-E. Olsson *et al.*, "Experimental validation of single BS 5G mmWave positioning and mapping for intelligent transport," *preprint arXiv:2303.11995*, 2023.

[20] D. T. Vu, A. Renaux, R. Boyer, and S. Marcos, "Performance analysis of 2D and 3D antenna arrays for source localization," in *Proc. Eur. Signal Process. Conf. (EUSIPCO)*, 2010, pp. 661–665.

[21] C. Lin and G. Y. Li, "Terahertz communications: An array-of-subarrays solution," *IEEE Commun. Mag.*, vol. 54, no. 12, pp. 124–131, 2016.

[22] S. Tarboush, H. Sarieddeen, H. Chen, M. H. Loukil, H. Jemaa, M.-S. Alouini, and T. Y. Al-Naffouri, "TeraMIMO: A channel simulator for wideband ultra-massive MIMO terahertz communications," *IEEE Trans. Veh. Technol.*, vol. 70, no. 12, pp. 12 325–12 341, 2021.

[23] X. Gao, L. Dai, S. Han, C.-L. I, and R. W. Heath, "Energy-efficient hybrid analog and digital precoding for mmWave MIMO systems with large antenna arrays," *IEEE J. Sel. Areas Commun.*, vol. 34, no. 4, pp. 998–1009, 2016.

[24] S. A. Busari, K. M. S. Huq, S. Mumtaz, J. Rodriguez, Y. Fang, D. C. Sicker, S. Al-Rubaye, and A. Tsourdos, "Generalized hybrid beamforming for vehicular connectivity using THz massive MIMO," *IEEE Trans. Veh. Technol.*, vol. 68, no. 9, pp. 8372–8383, 2019.

[25] N. Song, T. Yang, and H. Sun, "Overlapped subarray based hybrid beamforming for millimeter wave multiuser massive MIMO," *IEEE Signal Process Lett.*, vol. 24, no. 5, pp. 550–554, 2017.

[26] P. Zheng, T. Ballal, H. Chen, H. Wymeersch, and T. Y. Al-Naffouri, "Localization coverage analysis of THz communication systems with a 3D array," in *IEEE Global Communications Conference (GLOBECOM)*, 2022, pp. 5378–5383.

[27] T. Bai and R. W. Heath Jr, "Coverage and rate analysis for millimeter-wave cellular networks," *IEEE Trans. Wireless Commun.*, vol. 14, no. 2, pp. 1100–1114, 2015.

[28] N. R. Olson, J. G. Andrews, and R. W. Heath Jr, "Coverage and capacity of joint communication and sensing in wireless networks," *preprint arXiv:2210.02289*, 2022.

[29] N. Kouzayha, M. A. Kishk, H. Sarieddeen, M.-S. Alouini, and T. Y. Al-Naffouri, "Coexisting terahertz and RF finite wireless networks: Coverage and rate analysis," *IEEE Trans. Wireless Commun.*, vol. 22, no. 7, pp. 4873–4889, 2023.

[30] E. N. Papasotiriou, A.-A. A. Boulogeorgos, and A. Alexiou, "Fading modeling in indoor THz wireless systems," in *International Balkan Conference on Communications and Networking (BalkanCom)*, 2021, pp. 161–165.

[31] M. A. Nazari, G. Seco-Granados, P. Johannisson, and H. Wymeersch, "3D orientation estimation with multiple 5G mmWave base stations," in *Proc. IEEE Int. Conf. Commun. (ICC)*, 2021.

[32] M. Cui and L. Dai, "Channel estimation for extremely large-scale MIMO: Far-field or near-field?" *IEEE Trans. Commun.*, vol. 70, no. 4, pp. 2663–2677, 2022.

[33] N. Garcia, H. Wymeersch, and D. T. M. Slock, "Optimal precoders for tracking the AoD and AoA of a mmWave path," *IEEE Trans. Signal Process.*, vol. 66, no. 21, pp. 5718–5729, 2018.

[34] V. Petrov, M. Komarov, D. Moltchanov, J. M. Jornet, and Y. Koucheryavy, "Interference and SINR in millimeter wave and terahertz communication systems with blocking and directional antennas," *IEEE Trans. Commun.*, vol. 16, no. 3, pp. 1791–1808, 2017.

[35] D. Moltchanov, E. Sopin, V. Begishev, A. Samuylov, Y. Koucheryavy, and K. Samouylov, "A tutorial on mathematical modeling of 5G/6G millimeter wave and terahertz cellular systems," *IEEE Commun. Surv. Tutorials*, vol. 24, no. 2, pp. 1072–1116, 2022.

[36] A.-A. A. Boulogeorgos, E. N. Papasotiriou, and A. Alexiou, "Analytical performance assessment of THz wireless systems," *IEEE Access*, vol. 7, pp. 11 436–11 453, 2019.

[37] Y. Zhu, P.-Y. Kam, and Y. Xin, "On the mutual information distribution of MIMO Rician fading channels," *IEEE Trans. Commun.*, vol. 57, no. 5, pp. 1453–1462, 2009.

[38] S. Jin, X. Gao, and X. You, "On the ergodic capacity of rank-1 Ricean-fading MIMO channels," *IEEE Trans. Inf. Theory*, vol. 53, no. 2, pp. 502–517, 2007.

[39] F. R. Farrokhi, G. J. Foschini, A. Lozano, and R. A. Valenzuela, "Link-optimal space-time processing with multiple transmit and receive antennas," *IEEE Commun. Lett.*, vol. 5, no. 3, pp. 85–87, 2001.

[40] I. E. Gordon, L. S. Rothman, C. Hill, R. V. Kochanov, Y. Tan, P. F. Bernath, M. Birk, V. Boudon, A. Campargue, K. Chance *et al.*, "The HITRAN2016 molecular spectroscopic database," *J. Quant. Spectrosc. Radiat. Transfer*, vol. 203, pp. 3–69, 2017.

[41] J. M. Jornet and I. F. Akyildiz, "Channel modeling and capacity analysis for electromagnetic wireless nanonetworks in the terahertz band," *IEEE Trans. Wireless Commun.*, vol. 10, no. 10, pp. 3211–3221, 2011.

[42] F. Roemer, M. Haardt, and G. Del Galdo, "Analytical performance assessment of multi-dimensional matrix-and tensor-based ESPRIT-type algorithms," *IEEE Trans. Signal Process.*, vol. 62, no. 10, pp. 2611–2625, 2014.

[43] S. M. Kay, *Fundamentals of statistical signal processing: estimation theory*. Prentice-Hall, Inc., 1993.

[44] Z. Abu-Shaban, X. Zhou, T. Abhayapala, G. Seco-Granados, and H. Wymeersch, "Error bounds for uplink and downlink 3D localization in 5G millimeter wave systems," *IEEE Trans. Wireless Commun.*, vol. 17, no. 8, pp. 4939–4954, 2018.

[45] L. Liu, X. Zhang, and H. Ma, "Localization-oriented coverage in wireless camera sensor networks," *IEEE Trans. Wireless Commun.*, vol. 10, no. 2, pp. 484–494, 2011.

[46] O. M. Bushnaq, M. A. Kishk, A. Celik, M.-S. Alouini, and T. Y. Al-Naffouri, "Optimal deployment of tethered drones for maximum cellular coverage in user clusters," *IEEE Trans. Wireless Commun.*, vol. 20, no. 3, pp. 2092–2108, 2021.

[47] J. Li, L. C. Tran, and F. Safaei, "Outage probability and throughput analyses in full-duplex relaying systems with energy transfer," *IEEE Access*, vol. 8, pp. 150 150–150 161, 2020.

[48] S. Dang, J. P. Coon, and G. Chen, "Outage performance of two-hop OFDM systems with spatially random decode-and-forward relays," *IEEE Access*, vol. 5, pp. 27 514–27 524, 2017.

[49] A. Goldsmith, *Wireless communications*. Cambridge university press, 2005.

[50] L. Salaün, M. Coupechoux, and C. S. Chen, "Weighted sum-rate maximization in multi-carrier NOMA with cellular power constraint," in *INFOCOM*. IEEE, 2019, pp. 451–459.

[51] P.-A. Absil, R. Mahony, and R. Sepulchre, "Optimization algorithms on matrix manifolds," in *Optimization Algorithms on Matrix Manifolds*. Princeton University Press, 2009.

[52] N. Boumal, "An introduction to optimization on smooth manifolds," *Available online, May*, vol. 3, 2020.

[53] J. C. Gower and G. B. Dijksterhuis, *Procrustes problems*. OUP Oxford, 2004, vol. 30.

[54] D. Love and R. Heath, "Equal gain transmission in multiple-input multiple-output wireless systems," *IEEE Trans. Wireless Commun.*, vol. 51, no. 7, pp. 1102–1110, 2003.

[55] Z. Xiao, L. Bai, and J. Choi, "Iterative joint beamforming training with constant-amplitude phased arrays in millimeter-wave communications," *IEEE Commun. Lett.*, vol. 18, no. 5, pp. 829–832, 2014.

[56] E. N. Papasotiriou, A.-A. A. Boulogeorgos, K. Haneda, M. F. de Guzman, and A. Alexiou, "An experimentally validated fading model for THz wireless systems," *Sci. Rep.*, vol. 11, no. 1, p. 18717, 2021.

[57] K. A. Hamdi, "Capacity of MRC on correlated Rician fading channels," *IEEE Trans. Commun.*, vol. 56, no. 5, pp. 708–711, 2008.

[58] N. Boumal, B. Mishra, P.-A. Absil, and R. Sepulchre, "Manopt, a Matlab toolbox for optimization on manifolds," *Journal of Machine Learning Research*, vol. 15, no. 42, pp. 1455–1459, 2014. [Online]. Available: https://www.manopt.org